Global crustal thickness revealed by surface waves orbiting Mars

Doyeon Kim[1], Cecilia Duran[2], Domenico Giardini[2], Ana-Catalina Plesa[3], Simon C. Stähler[4], Christian Boehm[5], Vedran Lekic[6], Scott M. McLennan[7], Savas Ceylan[8], John Clinton[9], Paul McEwan Davis[10], Amir Khan[11], Brigitte Knapmeyer-Endrun[12], Mark Paul Panning[13], Mark A. Wieczorek[14], and Philippe Lognonné[15]

[1]Swiss Federal Institute of Technology in Zürich
[2]ETH Zürich
[3]German Aerospace Center
[4]Eidgenössische Technische Hochschule Zürich
[5]Department of Earth Sciences, Institute of Geophysics, ETH Zürich
[6]University of Maryland, College Park
[7]Stony Brook University
[8]ETH Zurich
[9]Swiss Seismological Service
[10]University of California Los Angeles
[11]Swiss Federal Institute of Technology
[12]Bensberg Observatory, University of Cologne
[13]Jet Propulsion Laboratory, California Institute of Technology
[14]Université Paris Cité
[15]Université Paris Cité, Institute de physique de globe de Paris, CNRS

March 6, 2023

Abstract

We report observations of Rayleigh waves that orbit around Mars up to three times following the S1222a marsquake. Averaging these signals, we find the largest amplitude signals at 30 s and 85 s central period, propagating with distinctly different group velocities of 2.9 km/s and 3.8 km/s, respectively. The group velocities constraining the average crustal thickness beneath the great circle path rule out the majority of previous crustal models of Mars that have a >200 kg/m3 density contrast across the dichotomy. We find that the thickness of the martian crust is 42-56 km on average, and thus thicker than the crusts of the Earth and Moon. Together with thermal evolution models, a thick martian crust suggests that the crust must contain 50-70% of the total heat production to explain present-day local melt zones in the interior of Mars.

Global Crustal Thickness Revealed by Surface Waves Orbiting Mars

D. Kim[1], C. Duran[1], D. Giardini[1], A-C. Plesa[2], S. C. Stähler[1,3], C. Boehm[1], V. Lekić[4], S. M. McLennan[5], S. Ceylan[1], J. F. Clinton[6], P. Davis[7], A. Khan[8], B. Knapmeyer-Endrun[9], M. P. Panning[10], M. Wieczorek[11], P. Lognonné[11]

[1]Institute of Geophysics, ETH Zurich, Switzerland
[2]DLR, Institute of Planetary Research, Berlin, Germany
[3]Physik-Institut, Universitä Zürich, Zurich, Switzerland
[4]Department of Geology, University of Maryland, College Park, USA
[5]Department of Geosciences, Stony Brook University, Stony Brook, USA
[6]Swiss Seismological Service, ETH Zurich, Zurich, Switzerland
[7]Department of Earth, Planetary, and Space Sciences, University of California Los Angeles, USA
[8]Institute of Geochemistry and Petrology, ETH Zurich, Zurich, Switzerland
[9]Bensberg Observatory, University of Cologne, Bergisch Gladbach, Germany
[10]Jet Propulsion Laboratory, California Institute of Technology, USA
[11]Université Paris Cité, Institut de physique du globe de Paris, CNRS, Paris, France

Key Points:

- We present the first observation of Rayleigh waves that orbit around Mars up to three times.
- Group velocity measurements and 3-D simulations constrain the average crustal and uppermost mantle velocities along the propagation path
- The global average crustal thickness is 42-56 km and requires a large enrichment of heat-producing elements to explain local melt zones

Corresponding author: D. Kim, doyeon.kim@erdw.ethz.ch

Abstract

We report observations of Rayleigh waves that orbit around Mars up to three times following the S1222a marsquake. Averaging these signals, we find the largest amplitude signals at 30 s and 85 s central period, propagating with distinctly different group velocities of 2.9 km/s and 3.8 km/s, respectively. The group velocities constraining the average crustal thickness beneath the great circle path rule out the majority of previous crustal models of Mars that have a >200 kg/m^3 density contrast across the dichotomy. We find that the thickness of the martian crust is 42-56 km on average, and thus thicker than the crusts of the Earth and Moon. Together with thermal evolution models, a thick martian crust suggests that the crust must contain 50-70% of the total heat production to explain present-day local melt zones in the interior of Mars.

Plain Language Summary

The NASA InSight mission and its seismometer installed on the surface of Mars is now retired after ∼4 years of operation. We observe clear seismic signals from surface waves called Rayleigh waves that orbit around Mars up to three times from the largest marsquake recording during the mission. By measuring the wavespeeds at which those surface waves travel in different frequencies, we obtain the first seismic evidence that constrains the average crustal and uppermost mantle structures beneath the traveling path on a planetary scale. Using the new seismic observations together with indirectly measured gravity data, we confirm the findings from our previous analyses of surface waves that the density of the crust in the northern lowlands and the southern highlands is similar or different by no more than 200 kg/m^3. Furthermore, we find the global average crustal thickness on Mars would be 42-56 km, much thicker than the Earth's and Moon's crusts. By exploring the thermal evolution of Mars, a thick martian crust requires about 50-70% of the heat-producing elements such as thorium, uranium, and potassium to be concentrated in the crust in order to explain local regions in the Martian mantle that can still undergo melting at present day.

1 Introduction

After more than 4 Earth years (∼1450 sols) of operations on the martian surface monitoring the planet's ground vibrations, the InSight mission (Banerdt et al., 2020) is now retired which leads to the end of its seismometer (SEIS; Lognonné et al., 2019) operation. Throughout the mission, analyses of body waves from marsquakes (Giardini et al., 2020; InSight Marsquake Service, 2022; Ceylan et al., 2022) and impacts (Garcia et al., 2022; Posiolova et al., 2022) have led to important discoveries about the planet's crust (Lognonné et al., 2020; Knapmeyer-Endrun et al., 2021; Kim, Lekić, et al., 2021), mantle (Khan et al., 2021; Durán et al., 2022; Drilleau et al., 2022), and core (Stähler et al., 2021; Khan et al., 2022; Irving et al., 2022). Recent detection of fundamental mode surface waves and overtones, together with gravimetric modeling enabled the characterization of crustal structure variations away from the InSight landing site and showed that average crustal velocity and density structure is similar between the northern lowlands and the southern highlands (Kim, Banerdt, et al., 2022; Kim, Stähler, et al., 2022).

Earlier in the mission, the InSight science team produced 1-D models of Mars' interior (KKS21; named after the three publications of Knapmeyer-Endrun et al., 2021; Khan et al., 2021; Stähler et al., 2021) by inverting travel times of the body wave arrivals together with geophysical and geodynamical parameters as a function of composition, temperature, and pressure at depth. Recently, cosmochemical constraints on the nature of the mantle (e.g., Khan et al., 2022) have been used to construct a unified description of the planetary structure that can explain both observed geophysical measurements as well as the major element distribution. Using an expanded body wave dataset and the new mantle composition of Mars, updated 1-D interior models of the planet are now available (e.g., Durán et al., 2022).

Despite different approaches and the new compositional constraints incorporated into the modeling, more than 75% of the seismic body wave measurements are predominantly sensitive to the lithospheric structure between the Elysium Planitia and the Cerberus Fossae where most of the planet's seismicity (Stähler et al., 2022) and small meteorite impacts have been observed (Garcia et al., 2022). Similarly, in those 1-D models, crustal structure directly beneath the landing site of InSight is assumed to be representative of average martian crust. These observational limitations and modeling choices can significantly bias our inferences of the global interior structure and dynamics of Mars.

In this study, we identify Rayleigh waves that orbit around Mars up to three full cycles (up to R7; Fig. 1A) and report their group velocity measurements for S1222a, the largest seismic event recorded by InSight. With long- (LP) and very-long-period (VLP) analysis of the R2-R7 and three-dimensional (3-D) wavefield simulations, we obtain seismic wavespeeds in average crustal and mantle structures and improve previously reported estimates on global crustal thickness on Mars. We highlight the implications of the new constraints from our analysis for the planet's interior structure and thermal evolution.

2 Data and Methods

The largest seismic event detected during the InSight mission is the M_W^{ma} 4.7 marsquake S1222a (Kawamura et al., 2022) (Fig. 1B). The seismic waveforms of S1222a contain both minor-arc Rayleigh and Love waves (e.g., Beghein et al., 2022), overtones (Kim, Stähler, et al., 2022), and Rayleigh waves that propagate around Mars for one cycle (R2 and R3) (e.g., Panning et al., 2023). To extend our analysis and search for Rayleigh waves traveling multiple times around Mars, we consider a 10-hour long seismic recording of S1222a (InSight Marsquake Service, 2023)(Fig. S1). We apply marsquake seismic data processing techniques to remove electro-mechanical noise by the sensor and the lander (Scholz et al., 2020), to suppress spurious signals and to avoid misinterpretation of the SEIS data (Kim, Davis, et al., 2021). We restrict our analysis to the 25 to 100 s period range because seismic energy observed outside this frequency range can be affected by atmospheric turbulence at various scales at longer periods (Banfield et al., 2020) or overprinted by strong scattering at shorter periods (van Driel et al., 2021; Karakostas et al., 2021). We correct for the presence of scattered waves in the seismic coda by examining frequency dependent polarization attributes (FDPAs) (e.g., Park et al., 1987). Here, we use the S-transform (Stockwell et al., 1996) of the three-component waveforms and calculate a 3 x 3 cross-component covariance matrix at each frequency in 80% overlapping time windows whose duration is inversely proportional to frequency. The relative sizes of the eigenvalues of this covariance matrix are related to the degree of polarization of the particle motion, while the complex-valued components of the eigenvectors describe the particle motion ellipsoid in each time-frequency window. To search for Rayleigh waves, we combine FDPAs to highlight seismic arrivals with elliptically-polarized particle motion predominantly in the vertical plane (Kim, Banerdt, et al., 2022). To further enhance the signal-to-noise ratio of our data, we shift a 200-s window across travel time predictions of the R2-R7 signals and perform a N-th root stacking (N=4) and assume that waves propagate along the great circle path (GCP), a commonly-made assumption in surface wave analysis on Earth (e.g., Moulik et al., 2022). We consider a range of GCPs based on the back azimuth uncertainties of the direct P-, S-waves, and minor-arc surface waves (Kawamura et al., 2022; Panning et al., 2023; Kim, Stähler, et al., 2022). Prediction windows for Rayleigh wave travel times are computed according to the depth sensitivity for each period range and the KKS21 model. The minor-arc Rayleigh wave (R1) is not included in the analysis to avoid producing a bias towards the minor-arc path. Here, we use a Hilbert envelope rather than the waveform to prevent distortion of seismic signals produced by nonlinear processing (e.g., Rost & Thomas, 2002).

Previously, little deviation for R1-R3 travel times in S1222a between the GCP and the ray theoretical path has been reported for existing crustal thickness models of Mars (Kim, Stähler, et al., 2022). To account for more realistic volumetric sensitivities for higher-orbit Rayleigh wave propagation, we carry out a 3-D wavefield simulation using the spectral-element method by Afanasiev et al. (2019). For our input model, we employ the 3-D crustal velocity modeling scheme used in the analysis of 3-D ray tracing by Kim, Stähler, et al. (2022). We produce a global crustal thickness map fixing the crustal thickness to 45 km at the InSight location using the gravimetric method by Wieczorek et al. (2022). The map used in this study has the crustal thickness ranges from 20 km to 90 km, the thinnest in Hellas and the thickest in the Tharsis province with an average thickness of 53 km (Fig. 1B). The initial crustal velocity profile is characterized by a positive velocity gradient of 0.02 km/s per km with an average shear velocity (V_S) of 3.2 km/s based on previous surface wave analyses of S1222a and the two large impacts, S1094b and S1000a (Fig. 1A). We assume a V_P/V_S ratio of 1.81 from the free-surface transform analysis in Kim, Lekić, et al. (2021). The 4-th order spectral-element mesh is constructed to globally resolve periods of 15 s at one element per wavelength, resulting in a total of 2.24 M elements. Variations in crustal thickness are modeled by deforming the outer layer of the unstructured mesh to align with surface and Moho topography. Within the crustal layer, the velocity profile is extrapolated and vertically scaled based on the distribution of crustal thickness range (e.g., Fig. 1B). For the mantle, we consider: (a) the 1-D reference velocity model of KKS21 (solid, Fig. 1A) and (b) the recently updated 1-D models that have a 5% faster uppermost mantle velocity resulting from a reduced mantle FeO content (hereafter Duran2022; dashed, Fig. 1A).

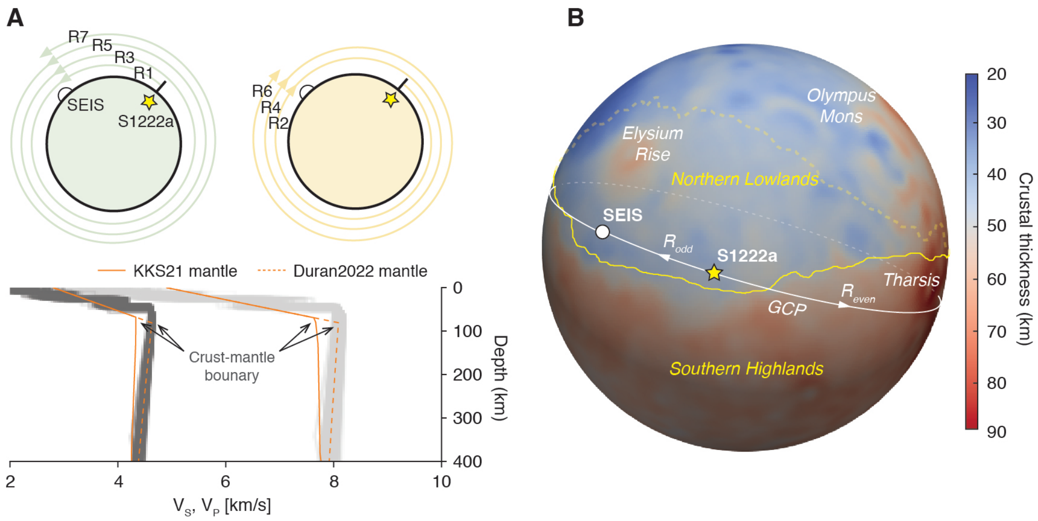

Figure 1. (**A**) Top diagram describes the direction of propagation and number of cycles for those surface waves orbiting around Mars in S1222a. Bottom shows 1-D interior models of Mars explored in this study. The crustal velocity profile constrained by previous surface wave studies are expanded to the existing mantle models of KKS21 (solid) and Duran2022 (dashed). For 3-D wavefield simulations, the two composite profiles are extrapolated by the thickness ranges shown in 1B. Gray profiles are the posterior distribution of models in Durán et al. (2022). (**B**) Crustal thickness distribution between the northern lowlands and southern highlands on Mars. S1222a and the lander locations are denoted by yelllow and white symbols, respectively. Background colormap denotes the crustal thickness used for generating our 3-D crustal velocity model of Mars. Dichotomy boundary (yellow dashed) is based on Andrews-Hanna et al. (2008). SEIS = InSight seismometer; GCP = Great circle path

3 Result and Discussion

Our LP (∼30 s) vertical-component envelope shows strong amplitude signals in the predicted time windows for R1, R2, and R3 traveling with an average group velocity range of 2.4-3.0 km/s (black curve, Fig. 2A). Weaker and more localized later-arrivals are observed within the predicted time windows for R4-R7. These arrivals appear to have relatively large elliptically-polarized energy in the vertical plane in the same period range (dashed brown, Fig. 2A). Linearly-polarized signals such as a small amplitude glitch (gray, Fig. 2A) or other body wave arrivals would show a negative correlation between envelope amplitude and the FDPA for Rayleigh waves. Arrivals outside the predicted windows may be associated with multipathing of the propagated surface waves in 3-D crustal structure or body-to-surface wave conversion. Whichever the case, these arrivals may have been contaminated by strong atmospheric noise as indicated by the lander modes (Dahmen et al., 2021) clearly visible during the 10-hour recording period (Fig. S1). For VLP (∼85 s), the envelope amplitude and the corresponding FDPA curve is highly correlated and both data show distinctive peaks observed up to the R6 window with a higher traveling speed of 3.6-4.0 km/s (Fig. 2B). Notably, the peak shown in the R3 window has the smallest amplitude and polarization across the peaks associated with R1-R6. The observed peak in the R7 window has a relatively large amplitude but is weakly polarized.

Averaging across the R2-R7 signals, we observe the strongest amplitude signals at 30 s and 85 s central periods, propagating with distinctively different group velocities of 2.9 km/s and 3.8 km/s, respectively, in both amplitude and polarization stacks (Fig. 2C-D). At 30 s, similar group velocities have been independently reported by other studies for the R2 and R3 arrivals in S1222a (Kim, Stähler, et al., 2022; Li et al., 2022; Panning et al., 2023). Unlike typical, smoothly-varying surface wave dispersion curves, as predicted by the existing 1-D models (e.g., Durán et al., 2022; Drilleau et al., 2022)(Fig. S2), the observed group velocities show an apparent jump at intermediate periods between 20 s and 100 s and do not appear to constructively interfere across multiple orbits of Mars (Fig. S3). Such abruptness in dispersion and the observed low and high velocities from the R2-R7 signals cannot be solely attributed by elliptically-polarized martian wind (e.g., Stutzmann et al., 2021) contaminating the data which is unlikely to be recorded with the apparent periodicity for both LP and VLP data. At much longer period between 100-200 s, a similar group velocity close to 3.8 km/s for the excitation of R2 has been reported by using ambient noise correlations (Deng & Levander, 2022). A normal mode study on Mars has also shown some potential excitation of the fundamental mode surface waves in comparable period ranges between 120-300 s (Lognonné et al., under review).

The predicted dispersion curves using a suite of 1-D models with varying crustal thickness illustrate that the two end-member group velocities at LP and VLP appear as a type of stationary phase or "Airy-phase" (Aki & Richards, 2002) across different periods (Fig. S4). Depending on crustal thickness in a model, however, the rise and fall of the velocities at intermediate periods will vary substantially and would not constructively interfere across multiple orbits of Mars. Such Airy-phase is often associated with the amplification of Rayleigh waves on Earth that can propagate for considerable distances across the continental crust (Ewing & Press, 1956) and mantle (Ewing & Press, 1954). The observation of Rayleigh waves traveling over multiple orbits on the seismic recording of a relatively small-magnitude quake (M_W^{ma} 4.6) suggests those stationary values of group velocities on Mars could be occurring close to 30 s and 85 s central periods.

Our 3-D wavefield simulations also show that large-scale variations in crustal thickness across the equatorial dichotomy are necessary to reproduce this behavior (Fig. S5-S6). Using our 3-D model, we find the spectra of the R2-R7 arrivals in synthetic waveform is largely discontinuous in time and frequency. This feature becomes more evident for Rayleigh waves propagating in higher-orbits beyond R3. The variation in amplitude

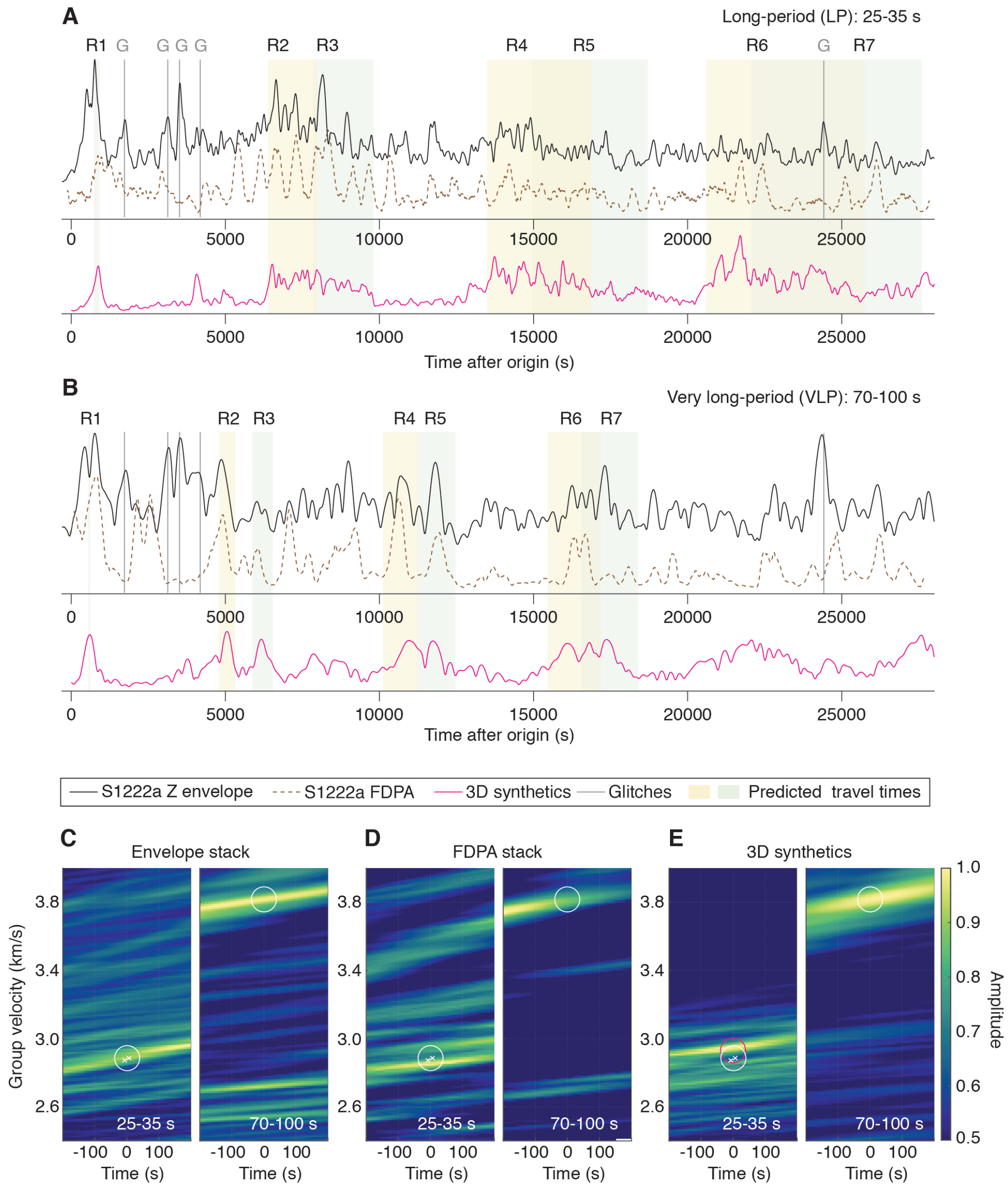

Figure 2. Vertical-component envelopes of the S1222a deglitched waveform (black) and FDPA (dashed brown) filtered between (**A**) 25-35 s (LP) and (**B**) 70-100 s periods (VLP). Shaded areas indicate the predicted time windows of R1-R7 arrivals base on the group velocities ranging from 2.4-3.0 km/s to 3.6-4.0 km/s for LP and VLP data, respectively. Glitches are shown by gray lines. Envelopes in magenta are based on a 3-D wavefield simulation using the model with crustal thickness variation shown in Fig. 1. Group velocity measurements of R2-R7 (white and magenta circles) are obtained by Nth-root stacking of the time-series in (A-B) for (**C-D**) data and (**E**) synthetics. White crosses are from independent analyses of R2 and R3 by Kim, Stähler, et al. (2022). See Fig. S3 for the complete analysis between 25-100 s with narrow-band filters. G = glitches; FDPA = frequency dependent polarization attribute

of surface waves propagating toward the minor-arc vs. major-arc directions (i.e., R_{odd} vs. R_{even}) also supports the evidence for lateral variation in crustal structure, likely due to (de)focusing of those waves (e.g., Romanowicz, 1987). Therefore, our observation of the absence of dispersion between ∼30-85 s for R2-R7 in S1222a and their associated amplitude change substantiate the choice of our 3-D model with large variation in crustal thickness (i.e., 20-90 km)(Fig. 1B) as these observations cannot be explained by existing 1-D models assuming a constant crustal thickness (Fig. S2).

The group velocity obtained for the largest amplitudes seen in the synthetic LP stack is consistent with our R2-R7 measurement of ∼2.9 km/s (with a small uncertainty of <2%; c.f., white and magenta symbols)(Fig. 2E), indicating that the average speed at which R2-R7 travel within the crust can be well-recovered with our 3-D model even with a large variation in crustal thickness (e.g., Fig. 1B). For the synthetic VLP stack, we find that the observed group velocity is strongly dependent on the versions of 1-D mantle models implemented in our analysis since the sensitivity of 70-100 s Rayleigh waves on Mars is predominantly between 75-115 km, a depth range in the uppermost mantle (Fig. S7). For example, the recent 1-D models produced by Durán et al. (2022) or Drilleau et al. (2022) have a 5% faster uppermost mantle than KKS21 (Fig. 1A). Our R2-R7 measurements are better fits to the newer sets of models that are based on a lower mantle FeO content compared to the KKS21 model that uses Wänke-Dreibus or Taylor compositions (Wänke et al., 1994; Taylor, 2013)(c.f., Fig. 2E and Fig. S8). This difference in seismic wavespeeds in existing models of the uppermost mantle, however, does not significantly affect body wave travel times with limited sensitivity and geographical coverage nor the estimated event locations (Fig. 3). Therefore, the new observations of R2-R7 provide a promising means of refining the 1-D models of the planet's radially symmetric structure, verifying the major element distribution of the martian mantle and determining the crustal thickness variations.

To find the average crustal thickness along the GCP from S1222a to the InSight lander, we carry out a systematic model-space search seeking average crustal V_S, thickness, and uppermost mantle V_S that fit the observed velocities of R2-R7 (Fig. 4A). We obtain a distribution of allowable velocities and thicknesses, with mean V_S of 3.38 km/s and 4.41 km/s for crustal and uppermost mantle, respectively, and a mean crustal thickness of 50 km beneath the GCP with an interquartile range between 44 and 58 km (magenta, Fig. 4A). This estimate of GCP-averaged crustal thickness and its uncertainty can be used as a robust anchoring-point and extrapolated globally using the existing models of crustal thickness based on gravimetric modeling (Wieczorek et al., 2022), which on their own suffer from a trade-off between average crustal density and thickness.

Crustal thickness directly beneath the lander based on RF analyses (Knapmeyer-Endrun et al., 2021; Kim, Lekić, et al., 2021) has previously been used as an anchoring-point to yield estimates of the average crustal thickness on Mars in the 30-72 km range. Here, we produce various crustal thickness models following the gravimetric modeling steps described in Wieczorek et al. (2022)(Fig. 4B). As an anchoring-point beneath the lander, we use the thickness of a three-layered crust ranging from 31 km to 47 km based on the previous RF analyses. Two end-member dichotomy structures with a uniform crustal density ranging from 2550 kg/m^3 to 3050 kg/m^3 (diamond symbol, Fig. 4B) and a model with a density contrast between 100-500 kg/m^3 across the dichotomy boundary have been tested (circle symbol, Fig. 4B). For the mantle and core beneath the lithosphere, we consider four plausible 1-D density profiles including both pre- and post-mission publications in Taylor (2013); Yoshizaki and McDonough (2020); Stähler et al. (2021); Khan et al. (2022).

Using the interquartile range of crustal thickness distribution along the GCP constrained by the R2-R7 analysis (magenta lines, Fig. 4A) against those from all models considered above, we were able to improve estimates of the average crustal thickness by ruling out the majority of those crustal models that have a >200 kg/m^3 density contrast

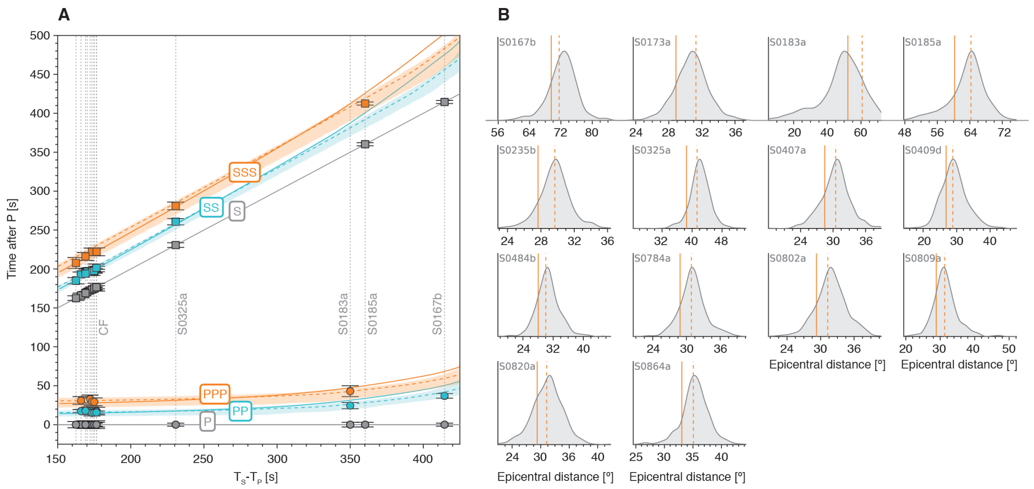

Figure 3. (**A**) Differential travel-time plot for available body wave measurements from quality A, B and C events and prediction by the inverted models of Durán et al. (2022)(shaded). Prediction by the composite models (Fig. 1B) with the mantle structure of KKS21 and the composite model with Duran2022 are shown by solid and dashed lines, respectively. Events are aligned by the their observed S-P travel time difference. Farside events (S0976a and S1000a; Horleston et al., 2022) are excluded since, besides the phases that allow for their alignment, no body-waves exclusive to the upper mantle and crustal structure were identified. CF = Cerberus Fossae event cluster. Note that the surface-reflected S-wave arrival (SS or SSS) of S0167b, categorized as a quality C event by the Marsquake Service (Clinton et al., 2021), was removed due to the lack of consensus on its nature (see Khan et al., 2021; Durán et al., 2022). (**B**) Distribution of the event distances from the inverted models in (Durán et al., 2022) (gray). Solid and dashed lines indicate the corresponding epicentral distances for the composite models (Fig. 1B) by fitting the predicted S-P travel times.

across the dichotomy (Fig. 4B). As a result, we obtain an estimate of the global average crustal thickness range between 42-56 km from the remaining models (symbols in magenta, Fig. 4B), which is a significantly narrower range than previously available. This implies large differences in crustal thickness between the northern lowlands and the southern highlands (up to ∼30 km), and places new constraints on the average global thickness of the martian crust, evidently thicker than the terrestrial (Dziewonski & Anderson, 1981; Huang et al., 2013) and the lunar crusts (Wieczorek et al., 2013) (Fig. 4C).

Of the major rocky bodies in the inner solar system for which constraints are available, Mars very likely has the thickest crust (i.e., 42-56 km). Based largely on seismic data, Earth's crust averages only about 24 km in thickness. The thickness of the lunar crust, which is anchored by Apollo seismic data, is in the range of 34-43 km (Wieczorek et al., 2013)(Fig. 4C). For the other bodies, there are no seismic data and crustal thickness constraints are based solely on gravity and topography measurements. Nevertheless, it is likely that on average, the thickness of the venusian crust is in the range of about 8-26 km (James et al., 2013; Maia & Wieczorek, 2022) and the mercurian crust in the range of 17-53 km (Padovan et al., 2015) or possibly even thinner (15-37 km; Sori, 2018). Even the crust of 4-Vesta may be broadly in this range with one estimate at 24 km (Ermakov et al., 2014). Accordingly, variations in crustal thicknesses of these rocky bodies appear to be within a factor of about 3-4 (McLennan, 2022). This is in contrast to planetary crustal masses which vary by well over an order of magnitude relative to the size of their

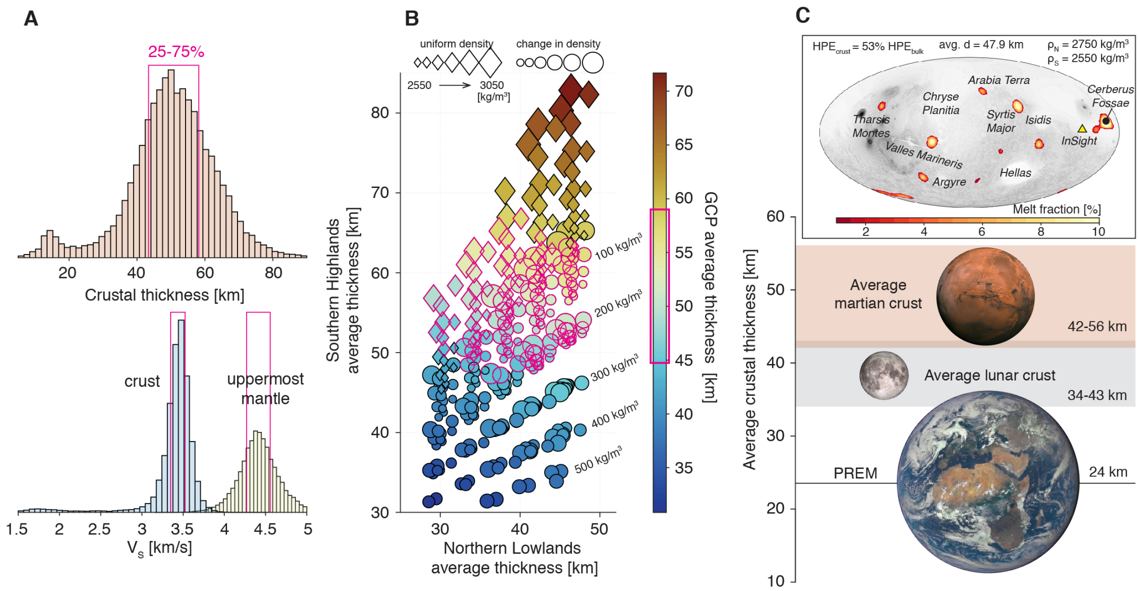

Figure 4. (**A**) Posterior distribution of the crustal and mantle V_S and crustal thickness along the GCP of S1222a. Interquartile range of the distribution is shown by red outlines. (**B**) Average crustal thickness of northern lowlands vs. southern highlands for global crustal thickness models with crustal densities ranging from 2550-3050 kg/m^3 with (circle symbol) and without a density contrast (diamond symbol) across the dichotomy. Dichotomy boundary is based on Andrews-Hanna et al. (2008). Colormap denotes the mean crustal thickness along the GCP for each model. Those models within the red outline are compatible with the posterior distribution in (A). (**C**) New global average crustal thickness range obtained by the model selection in (B) in comparison to that of the Earth and the Moon where constraints based on seismic data are available. Inset shows the best-fitting thermal evolution model of Plesa et al. (2018) computed with the new crustal constraint in (C). PREM = Preliminary Reference Earth Model. HPE = Heat-producing element

respective primitive mantles, between about 0.6% for Venus (and a similar value of 0.7% for Earth; Huang et al., 2013) to as much as 9.5% for Mercury and 14% for 4-Vesta (McLennan, 2022). Our results are consistent with Mars being intermediate among these values with the crust representing about 4-5% of the primitive mantle mass. Therefore, the degree of silicate differentiation into planetary crusts is more a function of overall planetary size than to crustal thickness and smaller bodies tend to have thicker crusts and increased degrees of mantle processing to form those crusts (O'Rourke & Korenaga, 2012; McLennan, 2022).

The tighter constraints on the crustal thickness obtained here compared to previously derived values from the RF analysis (Knapmeyer-Endrun et al., 2021) provide important information for thermal evolution models of the interior of Mars (Plesa et al., 2018, 2021; Khan et al., 2021; Knapmeyer-Endrun et al., 2021; Plesa et al., 2022). Together, this can help to further refine the president-day temperature distribution and amount of heat-producing elements within the crust. Thermal evolution models produced by using a maximum density contrast of <200 kg/m^3 across the dichotomy constrained by the R2-R7 analysis show that more than half of the total heat production but less than 70% of the total heat source budget needs to be in the crust, due to enrichment in the concentrations of Th, K, and U, in order to produce local melt zones in the mantle at present day (see detailed results in Fig. S9-S10). This crustal heat production range is consistent with the study of Knapmeyer-Endrun et al. (2021). For three end-member crustal models tested in Fig. S9-S10, we obtained enrichment factors between 8.2-14.3 (corresponding to a crustal heat production of 46.7-64.4 pW/kg). These enrichment factors are close to, but extend to slightly larger values than the enrichment estimated from GRS data 8 - 10.3 (crustal heat production of 46-51 pW/kg; Hahn et al., 2011). Interestingly, our best-fitting model with a 200 kg/m^3 variable density favors mantle plumes that can produce melt up to the present day in and around Cerberus Fossae (inset, Fig. 4D), supporting the interpretation from gravity and topography data (Broquet & Andrews-Hanna, 2022) and from seismic observations (Stähler et al., 2022). Therefore, our study offers a promising opportunity for further evaluating the plume hypothesis beneath Cerberus Fossae.

4 Open Research

The InSight event catalogue `https://doi.org/10.12686/a17` and waveform data are available from the IRIS-DMC `http://ds.iris.edu/ds/nodes/dmc/tools/mars-events/`, NASA-PDS `https://pds-geosciences.wustl.edu/missions/insight/seis.htm` and IPGP data center `https://doi.org/10.18715/SEIS.INSIGHT.XB_2016`.

Acknowledgments
This paper is InSight contribution number 315. The authors acknowledge the NASA, the CNES, their partner agencies and Institutions (UKSA, SSO, DLR, JPL, IPGP-CNRS, ETHZ, IC, and MPS-MPG) and the flight operations team at JPL, SISMOC, MSDS, IRIS-DMC, and PDS for providing the SEED SEIS data. Marsquake Service (MQS) operations at ETH are supported by ETH Research grant ETH-06 17-02. ETH authors recognize support from the ETH+ funding scheme (ETH+02 19-1: "Planet Mars"). V.L. acknowledge funding from NASA grant 80NSSC18K1628 and NASA Solar System Exploration Research Virtual Institute (SSERVI) Cooperative Agreement 80NSSC19M0216. SMM acknowledges funding from NASA grant 80NSSC18K1622.

References

Afanasiev, M., Boehm, C., van Driel, M., Krischer, L., Rietmann, M., May, D. A., ... Fichtner, A. (2019). Modular and flexible spectral-element waveform modelling in two and three dimensions. *Geophysical Journal International*, *216*(3), 1675–1692.

Aki, K., & Richards, P. G. (2002). *Quantitative seismology.*

Andrews-Hanna, J. C., Zuber, M. T., & Banerdt, W. B. (2008). The borealis basin and the origin of the martian crustal dichotomy. *Nature*, *453*(7199), 1212–1215.

Banerdt, W. B., Smrekar, S. E., Banfield, D., Giardini, D., Golombek, M., Johnson, C. L., ... et al. (2020). Initial results from the insight mission on mars. *Nature Geoscience*, *13*(3), 183–189.

Banfield, D., Spiga, A., Newman, C., Forget, F., Lemmon, M., Lorenz, R., ... et al. (2020). The atmosphere of mars as observed by insight. *Nature Geoscience*, *13*(3), 190–198.

Beghein, C., Li, J., Weidner, E., Maguire, R., Wookey, J., Lekić, V., ... Banerdt, W. (2022). Crustal anisotropy in the martian lowlands from surface waves. *Geophysical Research Letters*, *49*(24), e2022GL101508.

Broquet, A., & Andrews-Hanna, J. C. (2022). Geophysical evidence for an active mantle plume underneath elysium planitia on mars. *Nature Astronomy*, 1–10.

Ceylan, S., Clinton, J. F., Giardini, D., Stähler, S. C., Horleston, A., Kawamura, T., ... et al. (2022). The marsquake catalogue from insight, sols 0–1011. *Physics* *of the Earth and Planetary Interiors*, *333*, 106943.

Clinton, J. F., Ceylan, S., van Driel, M., Giardini, D., Stähler, S. C., Böse, M., ... et al. (2021). The marsquake catalogue from insight, sols 0–478. *Physics of the Earth and Planetary Interiors*, *310*, 106595.

Dahmen, N. L., Zenhäusern, G., Clinton, J. F., Giardini, D., Stähler, S. C., Ceylan, S., ... Banerdt, W. B. (2021, 10). Resonances and Lander Modes Observed by InSight on Mars (1–9 Hz). *Bulletin of the Seismological Society of America*, *111*(6), 2924-2950. doi: 10.1785/0120210056

Deng, S., & Levander, A. (2022). Autocorrelation r2 on mars. *Geophysical Research Letters*, *49*(17), e2022GL099580.

Drilleau, M., Samuel, H., Garcia, R. F., Rivoldini, A., Perrin, C., Michaut, C., ... et al. (2022). Marsquake locations and 1-d seismic models for mars from insight data. *Journal of Geophysical Research: Planets*, *127*(9), e2021JE007067.

Durán, C., Khan, A., Ceylan, S., Zenhäusern, G., Staehler, S., Clinton, J., & Giardini, D. (2022). Seismology on mars: An analysis of direct, reflected, and converted seismic body waves with implications for interior structure. *Physics of the Earth and Planetary Interiors*, *325*, 106851.

Dziewonski, A. M., & Anderson, D. L. (1981). Preliminary reference earth model. *Physics of the earth and planetary interiors*, *25*(4), 297–356.

Ermakov, A. I., Zuber, M. T., Smith, D. E., Raymond, C. A., Balmino, G., Fu, R. R., & Ivanov, B. A. (2014). Constraints on vesta's interior structure using gravity and shape models from the dawn mission. *Icarus*, *240*, 146–160.

Ewing, M., & Press, F. (1954). An investigation of mantle rayleigh waves. *Bulletin of the Seismological Society of America*, *44*(2A), 127–147.

Ewing, M., & Press, F. (1956). Rayleigh wave dispersion in the period range 10 to 500 seconds. *Eos, Transactions American Geophysical Union*, *37*(2), 213–215.

Garcia, R. F., Daubar, I. J., Beucler, É., Posiolova, L. V., Collins, G. S., Lognonné, P., ... et al. (2022). Newly formed craters on mars located using seismic and acoustic wave data from insight. *Nature Geoscience*, *15*(10), 774–780.

Giardini, D., Lognonné, P., Banerdt, W. B., Pike, W. T., Christensen, U., Ceylan, S., ... Yana, C. (2020). The Seismicity of Mars. *Nat. Geosci.*. doi: 10.1038/s41561-020-0539-8

Hahn, B., McLennan, S., & Klein, E. (2011). Martian surface heat production and crustal heat flow from Mars Odyssey Gamma-Ray spectrometry. *Geophysical Research Letters*, *38*(14).

Horleston, A. C., Clinton, J. F., Ceylan, S., Giardini, D., Charalambous, C., Irving, J. C. E., ... Banerdt, W. B. (2022, 04). The Far Side of Mars: Two Distant Marsquakes Detected by InSight. *The Seismic Record*, *2*(2), 88-99. doi: 10.1785/0320220007

Huang, Y., Chubakov, V., Mantovani, F., Rudnick, R. L., & McDonough, W. F. (2013). A reference earth model for the heat-producing elements and associated geoneutrino flux. *Geochemistry, Geophysics, Geosystems*, *14*(6), 2003–2029.

InSight Marsquake Service. (2022). *Mars Seismic Catalogue, InSight Mission; V3 2020-07-01. ETHZ, IPGP, JPL, ICL, ISAE-Supaero, MPS, Univ Bristol. Dataset.* doi: https://doi.org/10.12686/a19

InSight Marsquake Service. (2023). *Mars seismic catalogue, insight mission; v13 2023-01-01.* ETHZ, IPGP, JPL, ICL, Univ. Bristol. Retrieved from `https://www.insight.ethz.ch/seismicity/catalog/v13` doi: 10.12686/a19

Irving, J., Antonangeli, D., Banerdt, B., Li, J., Bozdag, E., Stähler, S., ... Stutzmann, E. (2022, 01). First observations of seismic waves travelling through the martian core..

James, P. B., Zuber, M. T., & Phillips, R. J. (2013). Crustal thickness and support of topography on venus. *Journal of Geophysical Research: Planets*, *118*(4), 859–875.

Karakostas, F., Schmerr, N., Maguire, R., Huang, Q., Kim, D., Lekic, V., ... others (2021). Scattering attenuation of the martian interior through coda-wave analysis. *Bulletin of the Seismological Society of America*, *111*(6), 3035–3054.

Kawamura, T., Clinton, J. F., Zenhäusern, G., Ceylan, S., Horleston, A. C., Dahmen, N. L., ... Banerdt, W. B. (2022). S1222a - the largest marsquake detected by insight. *Geophysical Research Letters*, e2022GL101543. doi: https://doi.org/10.1029/2022GL101543

Khan, A., Ceylan, S., van Driel, M., Giardini, D., Lognonné, P., Samuel, H., ... et al. (2021). Upper mantle structure of mars from insight seismic data. *Science*, *373*(6553), 434–438.

Khan, A., Sossi, P. A., Liebske, C., Rivoldini, A., & Giardini, D. (2022). Geophysical and cosmochemical evidence for a volatile-rich mars. *Earth and Planetary Science Letters*, *578*, 117330.

Kim, D., Banerdt, W., Ceylan, S., Giardini, D., Lekić, V., Lognonné, P., ... et al. (2022). Surface waves and crustal structure on mars. *Science*, *378*(6618), 417–421.

Kim, D., Davis, P., Lekić, V., Maguire, R., Compaire, N., Schimmel, M., ... et al. (2021). Potential pitfalls in the analysis and structural interpretation of seismic data from the mars insight mission. *Bulletin of the Seismological Society of America*, *111*(6), 2982–3002.

Kim, D., Lekić, V., Irving, J. C., Schmerr, N., Knapmeyer-Endrun, B., Joshi, R., ... et al. (2021). Improving constraints on planetary interiors with pps receiver functions. *Journal of Geophysical Research: Planets*, *126*(11), e2021JE006983.

Kim, D., Stähler, S., Ceylan, S., Lekic, V., Maguire, R., Zenhäusern, G., ... et al. (2022). Structure along the martian dichotomy constrained by rayleigh and love waves and their overtones. *Geophysical Research Letters*, e2022GL101666.

Knapmeyer-Endrun, B., Panning, M. P., Bissig, F., Joshi, R., Khan, A., Kim, D., ... et al. (2021). Thickness and structure of the martian crust from insight seismic data. *Science*, *373*(6553), 438–443.

Li, J., Beghein, C., Lognonné, P., McLennan, S. M., Wieczorek, M., Panning, M., ... Banerdt, W. B. (2022). Different martian crustal seismic velocities across the dichotomy boundary from multi-orbiting surface waves. *Geophysical Research Letters*, e2022GL101243.

Lognonné, P., Banerdt, W. B., Giardini, D., Pike, W. T., Christensen, U., Laudet, P., ... et al. (2019). Seis: Insight's seismic experiment for internal structure of mars. *Space Science Reviews*, *215*, 1–170.

Lognonné, P., Schimmel, M., Stutzmann, E., Davis, P., Drilleau, M., Sainton, G., ... Panning, B. W. B., M. P. (under review). Detection of mars normal modes from s1222 event and seismic noise. *Geophysical Research Letters*.

Lognonné, P., Banerdt, W., Pike, W., Giardini, D., Christensen, U., Garcia, R., ... Zweifel, P. (2020). Constraints on the shallow elastic and anelastic structure of Mars from InSight seismic data. *Nat. Geosci.*. doi: 10.1038/s41561-020-0536-y

Maia, J. S., & Wieczorek, M. A. (2022). Lithospheric structure of venusian crustal plateaus. *Journal of Geophysical Research: Planets*, *127*(2), e2021JE007004.

McLennan, S. M. (2022). Composition of planetary crusts and planetary differentiation. In *Planetary volcanism across the solar system* (pp. 287–331). Elsevier.

Moulik, P., Lekic, V., Romanowicz, B., Ma, Z., Schaeffer, A., Ho, T., ... others (2022). Global reference seismological data sets: multimode surface wave dispersion. *Geophysical Journal International*, *228*(3), 1808–1849.

O'Rourke, J. G., & Korenaga, J. (2012). Terrestrial planet evolution in the stagnant-lid regime: Size effects and the formation of self-destabilizing crust. *Icarus*, *221*(2), 1043–1060.

Padovan, S., Wieczorek, M. A., Margot, J.-L., Tosi, N., & Solomon, S. C. (2015). Thickness of the crust of mercury from geoid-to-topography ratios. *Geophysical*

Research Letters, *42*(4), 1029–1038.

Panning, M. P., Banerdt, W. B., Beghein, C., Carrasco, S., Ceylan, S., Clinton, J. F., … Zenhäusern, G. (2023). Locating the largest event observed on mars with multi-orbit surface waves. *Geophysical Research Letters*, *50*(1), e2022GL101270. doi: https://doi.org/10.1029/2022GL101270

Park, J., Vernon III, F. L., & Lindberg, C. R. (1987). Frequency dependent polarization analysis of high-frequency seismograms. *Journal of Geophysical Research: Solid Earth*, *92*(B12), 12664–12674.

Plesa, A.-C., Bozdağ, E., Rivoldini, A., Knapmeyer, M., McLennan, S. M., Padovan, S., … Spohn, T. (2021). Seismic velocity variations in a 3d martian mantle: Implications for the insight measurements. *Journal of Geophysical Research: Planets*, *126*(6), e2020JE006755. doi: https://doi.org/10.1029/2020JE006755

Plesa, A.-C., Padovan, S., Tosi, N., Breuer, D., Grott, M., Wieczorek, M., … Banerdt, W. (2018). The thermal state and interior structure of Mars. *Geophysical Research Letters*, *45*(22), 12–198.

Plesa, A.-C., Wieczorek, M., Knapmeyer, M., Rivoldini, A., Walterova, M., & Breuer, D. (2022). Interior dynamics and thermal evolution of mars–a geodynamic perspective. *Geophysical Exploration of the Solar System*, *63*, 179–230.

Posiolova, L. V., Lognonné, P., Banerdt, W. B., Clinton, J., Collins, G. S., Kawamura, T., … Zenhäusern, G. (2022). Largest recent impact craters on mars: Orbital imaging and surface seismic co-investigation. *Science*, *378*(6618), 412-417. doi: 10.1126/science.abq7704

Romanowicz, B. (1987). Multiplet-multiplet coupling due to lateral heterogeneity: asymptotic effects on the amplitude and frequency of the earth's normal modes. *Geophysical Journal International*, *90*(1), 75–100.

Rost, S., & Thomas, C. (2002). Array seismology: Methods and applications. *Reviews of geophysics*, *40*(3), 2–1.

Scholz, J.-R., Widmer-Schnidrig, R., Davis, P., Lognonné, P., Pinot, B., Garcia, R. F., … Banerdt, W. B. (2020). Detection, analysis, and removal of glitches from insight's seismic data from mars. *Earth and Space Science*, *7*(11), e2020EA001317. doi: https://doi.org/10.1029/2020EA001317

Sori, M. M. (2018). A thin, dense crust for mercury. *Earth and Planetary Science Letters*, *489*, 92–99.

Stähler, S. C., Khan, A., Banerdt, W. B., Lognonné, P., Giardini, D., Ceylan, S., … et al. (2021). Seismic detection of the martian core. *Science*, *373*(6553), 443–448.

Stähler, S. C., Mittelholz, A., Perrin, C., Kawamura, T., Kim, D., Knapmeyer, M., … et al. (2022). Tectonics of cerberus fossae unveiled by marsquakes. *Nature Astronomy*, 1–11.

Stockwell, R. G., Mansinha, L., & Lowe, R. (1996). Localization of the complex spectrum: the s transform. *IEEE transactions on signal processing*, *44*(4), 998–1001.

Stutzmann, E., Schimmel, M., Lognonné, P., Horleston, A., Ceylan, S., van Driel, M., … Spiga, A. (2021). The polarization of ambient noise on mars. *Journal of Geophysical Research: Planets*, *126*(1), e2020JE006545. doi: https://doi.org/10.1029/2020JE006545

Taylor, G. J. (2013). The bulk composition of mars. *Geochemistry*, *73*(4), 401–420.

van Driel, M., Ceylan, S., Clinton, J. F., Giardini, D., Horleston, A., Margerin, L., … others (2021). High-frequency seismic events on mars observed by insight. *Journal of Geophysical Research: Planets*, *126*(2), e2020JE006670.

Wieczorek, M. A., Broquet, A., McLennan, S. M., Rivoldini, A., Golombek, M., Antonangeli, D., … Banerdt, W. B. (2022). Insight constraints on the global character of the martian crust. *Journal of Geophysical Research: Planets*, *127*(5), e2022JE007298. doi: https://doi.org/10.1029/2022JE007298

Wieczorek, M. A., Neumann, G. A., Nimmo, F., Kiefer, W. S., Taylor, G. J., Melosh, H. J., ... Zuber, M. T. (2013). The crust of the moon as seen by grail. *Science*, *339*(6120), 671-675. doi: 10.1126/science.1231530

Wänke, H., Dreibus, G., Wright, I. P., Cowley, S. W. H., Runcorn, S. K., & Southwood, D. J. (1994). Chemistry and accretion history of mars. *Philosophical Transactions of the Royal Society of London. Series A: Physical and Engineering Sciences*, *349*(1690), 285-293. doi: 10.1098/rsta.1994.0132

Yoshizaki, T., & McDonough, W. F. (2020). The composition of mars. *Geochimica et Cosmochimica Acta*, *273*, 137–162.

Global Crustal Thickness Revealed by Surface Waves Orbiting Mars

D. Kim[1], C. Duran[1], D. Giardini[1], A-C. Plesa[2], S. C. Stähler[1,3], C. Boehm[1], V. Lekić[4], S. M. McLennan[5], S. Ceylan[1], J. F. Clinton[6], P. Davis[7], A. Khan[8], B. Knapmeyer-Endrun[9], M. P. Panning[10], M. Wieczorek[11], P. Lognonné[11]

[1]Institute of Geophysics, ETH Zurich, Switzerland
[2]DLR, Institute of Planetary Research, Berlin, Germany
[3]Physik-Institut, Universitä Zürich, Zurich, Switzerland
[4]Department of Geology, University of Maryland, College Park, USA
[5]Department of Geosciences, Stony Brook University, Stony Brook, USA
[6]Swiss Seismological Service, ETH Zurich, Zurich, Switzerland
[7]Department of Earth, Planetary, and Space Sciences, University of California Los Angeles, USA
[8]Institute of Geochemistry and Petrology, ETH Zurich, Zurich, Switzerland
[9]Bensberg Observatory, University of Cologne, Bergisch Gladbach, Germany
[10]Jet Propulsion Laboratory, California Institute of Technology, USA
[11]Université Paris Cité, Institut de physique du globe de Paris, CNRS, Paris, France

Key Points:

- We present the first observation of Rayleigh waves that orbit around Mars up to three times.
- Group velocity measurements and 3-D simulations constrain the average crustal and uppermost mantle velocities along the propagation path
- The global average crustal thickness is 42-56 km and requires a large enrichment of heat-producing elements to explain local melt zones

Corresponding author: D. Kim, `doyeon.kim@erdw.ethz.ch`

Abstract

We report observations of Rayleigh waves that orbit around Mars up to three times following the S1222a marsquake. Averaging these signals, we find the largest amplitude signals at 30 s and 85 s central period, propagating with distinctly different group velocities of 2.9 km/s and 3.8 km/s, respectively. The group velocities constraining the average crustal thickness beneath the great circle path rule out the majority of previous crustal models of Mars that have a >200 kg/m^3 density contrast across the dichotomy. We find that the thickness of the martian crust is 42-56 km on average, and thus thicker than the crusts of the Earth and Moon. Together with thermal evolution models, a thick martian crust suggests that the crust must contain 50-70% of the total heat production to explain present-day local melt zones in the interior of Mars.

Plain Language Summary

The NASA InSight mission and its seismometer installed on the surface of Mars is now retired after ∼4 years of operation. We observe clear seismic signals from surface waves called Rayleigh waves that orbit around Mars up to three times from the largest marsquake recording during the mission. By measuring the wavespeeds at which those surface waves travel in different frequencies, we obtain the first seismic evidence that constrains the average crustal and uppermost mantle structures beneath the traveling path on a planetary scale. Using the new seismic observations together with indirectly measured gravity data, we confirm the findings from our previous analyses of surface waves that the density of the crust in the northern lowlands and the southern highlands is similar or different by no more than 200 kg/m^3. Furthermore, we find the global average crustal thickness on Mars would be 42-56 km, much thicker than the Earth's and Moon's crusts. By exploring the thermal evolution of Mars, a thick martian crust requires about 50-70% of the heat-producing elements such as thorium, uranium, and potassium to be concentrated in the crust in order to explain local regions in the Martian mantle that can still undergo melting at present day.

1 Introduction

After more than 4 Earth years (∼1450 sols) of operations on the martian surface monitoring the planet's ground vibrations, the InSight mission (Banerdt et al., 2020) is now retired which leads to the end of its seismometer (SEIS; Lognonné et al., 2019) operation. Throughout the mission, analyses of body waves from marsquakes (Giardini et al., 2020; InSight Marsquake Service, 2022; Ceylan et al., 2022) and impacts (Garcia et al., 2022; Posiolova et al., 2022) have led to important discoveries about the planet's crust (Lognonné et al., 2020; Knapmeyer-Endrun et al., 2021; Kim, Lekić, et al., 2021), mantle (Khan et al., 2021; Durán et al., 2022; Drilleau et al., 2022), and core (Stähler et al., 2021; Khan et al., 2022; Irving et al., 2022). Recent detection of fundamental mode surface waves and overtones, together with gravimetric modeling enabled the characterization of crustal structure variations away from the InSight landing site and showed that average crustal velocity and density structure is similar between the northern lowlands and the southern highlands (Kim, Banerdt, et al., 2022; Kim, Stähler, et al., 2022).

Earlier in the mission, the InSight science team produced 1-D models of Mars' interior (KKS21; named after the three publications of Knapmeyer-Endrun et al., 2021; Khan et al., 2021; Stähler et al., 2021) by inverting travel times of the body wave arrivals together with geophysical and geodynamical parameters as a function of composition, temperature, and pressure at depth. Recently, cosmochemical constraints on the nature of the mantle (e.g., Khan et al., 2022) have been used to construct a unified description of the planetary structure that can explain both observed geophysical measurements as well as the major element distribution. Using an expanded body wave dataset and the new mantle composition of Mars, updated 1-D interior models of the planet are now available (e.g., Durán et al., 2022).

Despite different approaches and the new compositional constraints incorporated into the modeling, more than 75% of the seismic body wave measurements are predominantly sensitive to the lithospheric structure between the Elysium Planitia and the Cerberus Fossae where most of the planet's seismicity (Stähler et al., 2022) and small meteorite impacts have been observed (Garcia et al., 2022). Similarly, in those 1-D models, crustal structure directly beneath the landing site of InSight is assumed to be representative of average martian crust. These observational limitations and modeling choices can significantly bias our inferences of the global interior structure and dynamics of Mars.

In this study, we identify Rayleigh waves that orbit around Mars up to three full cycles (up to R7; Fig. 1A) and report their group velocity measurements for S1222a, the largest seismic event recorded by InSight. With long- (LP) and very-long-period (VLP) analysis of the R2-R7 and three-dimensional (3-D) wavefield simulations, we obtain seismic wavespeeds in average crustal and mantle structures and improve previously reported estimates on global crustal thickness on Mars. We highlight the implications of the new constraints from our analysis for the planet's interior structure and thermal evolution.

2 Data and Methods

The largest seismic event detected during the InSight mission is the M_W^{ma} 4.7 marsquake S1222a (Kawamura et al., 2022) (Fig. 1B). The seismic waveforms of S1222a contain both minor-arc Rayleigh and Love waves (e.g., Beghein et al., 2022), overtones (Kim, Stähler, et al., 2022), and Rayleigh waves that propagate around Mars for one cycle (R2 and R3) (e.g., Panning et al., 2023). To extend our analysis and search for Rayleigh waves traveling multiple times around Mars, we consider a 10-hour long seismic recording of S1222a (InSight Marsquake Service, 2023)(Fig. S1). We apply marsquake seismic data processing techniques to remove electro-mechanical noise by the sensor and the lander (Scholz et al., 2020), to suppress spurious signals and to avoid misinterpretation of the SEIS data (Kim, Davis, et al., 2021). We restrict our analysis to the 25 to 100 s period range because seismic energy observed outside this frequency range can be affected by atmospheric turbulence at various scales at longer periods (Banfield et al., 2020) or overprinted by strong scattering at shorter periods (van Driel et al., 2021; Karakostas et al., 2021). We correct for the presence of scattered waves in the seismic coda by examining frequency dependent polarization attributes (FDPAs) (e.g., Park et al., 1987). Here, we use the S-transform (Stockwell et al., 1996) of the three-component waveforms and calculate a 3 x 3 cross-component covariance matrix at each frequency in 80% overlapping time windows whose duration is inversely proportional to frequency. The relative sizes of the eigenvalues of this covariance matrix are related to the degree of polarization of the particle motion, while the complex-valued components of the eigenvectors describe the particle motion ellipsoid in each time-frequency window. To search for Rayleigh waves, we combine FDPAs to highlight seismic arrivals with elliptically-polarized particle motion predominantly in the vertical plane (Kim, Banerdt, et al., 2022). To further enhance the signal-to-noise ratio of our data, we shift a 200-s window across travel time predictions of the R2-R7 signals and perform a N-th root stacking (N=4) and assume that waves propagate along the great circle path (GCP), a commonly-made assumption in surface wave analysis on Earth (e.g., Moulik et al., 2022). We consider a range of GCPs based on the back azimuth uncertainties of the direct P-, S-waves, and minor-arc surface waves (Kawamura et al., 2022; Panning et al., 2023; Kim, Stähler, et al., 2022). Prediction windows for Rayleigh wave travel times are computed according to the depth sensitivity for each period range and the KKS21 model. The minor-arc Rayleigh wave (R1) is not included in the analysis to avoid producing a bias towards the minor-arc path. Here, we use a Hilbert envelope rather than the waveform to prevent distortion of seismic signals produced by nonlinear processing (e.g., Rost & Thomas, 2002).

Previously, little deviation for R1-R3 travel times in S1222a between the GCP and the ray theoretical path has been reported for existing crustal thickness models of Mars (Kim, Stähler, et al., 2022). To account for more realistic volumetric sensitivities for higher-orbit Rayleigh wave propagation, we carry out a 3-D wavefield simulation using the spectral-element method by Afanasiev et al. (2019). For our input model, we employ the 3-D crustal velocity modeling scheme used in the analysis of 3-D ray tracing by Kim, Stähler, et al. (2022). We produce a global crustal thickness map fixing the crustal thickness to 45 km at the InSight location using the gravimetric method by Wieczorek et al. (2022). The map used in this study has the crustal thickness ranges from 20 km to 90 km, the thinnest in Hellas and the thickest in the Tharsis province with an average thickness of 53 km (Fig. 1B). The initial crustal velocity profile is characterized by a positive velocity gradient of 0.02 km/s per km with an average shear velocity (V_S) of 3.2 km/s based on previous surface wave analyses of S1222a and the two large impacts, S1094b and S1000a (Fig. 1A). We assume a V_P/V_S ratio of 1.81 from the free-surface transform analysis in Kim, Lekić, et al. (2021). The 4-th order spectral-element mesh is constructed to globally resolve periods of 15 s at one element per wavelength, resulting in a total of 2.24 M elements. Variations in crustal thickness are modeled by deforming the outer layer of the unstructured mesh to align with surface and Moho topography. Within the crustal layer, the velocity profile is extrapolated and vertically scaled based on the distribution of crustal thickness range (e.g., Fig. 1B). For the mantle, we consider: (a) the 1-D reference velocity model of KKS21 (solid, Fig. 1A) and (b) the recently updated 1-D models that have a 5% faster uppermost mantle velocity resulting from a reduced mantle FeO content (hereafter Duran2022; dashed, Fig. 1A).

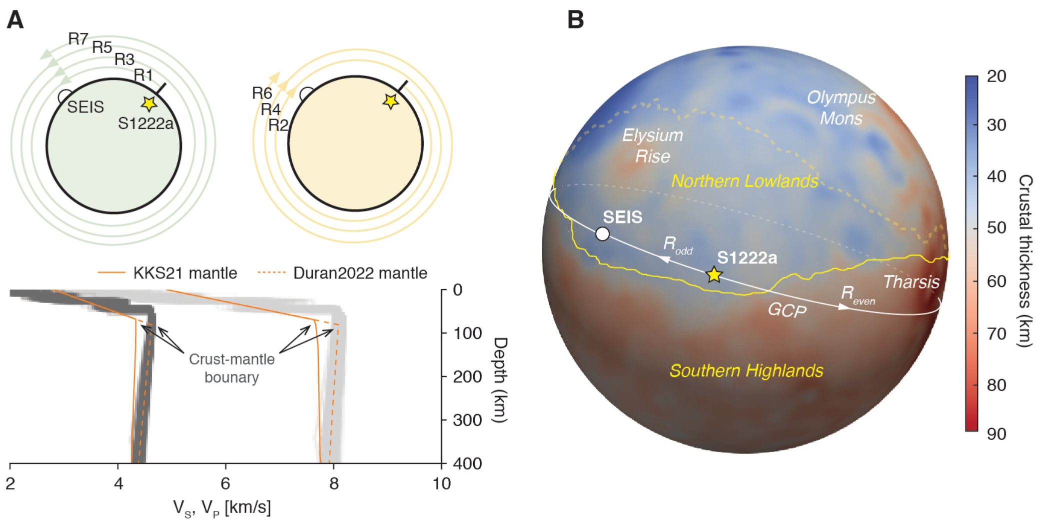

Figure 1. (**A**) Top diagram describes the direction of propagation and number of cycles for those surface waves orbiting around Mars in S1222a. Bottom shows 1-D interior models of Mars explored in this study. The crustal velocity profile constrained by previous surface wave studies are expanded to the existing mantle models of KKS21 (solid) and Duran2022 (dashed). For 3-D wavefield simulations, the two composite profiles are extrapolated by the thickness ranges shown in 1B. Gray profiles are the posterior distribution of models in Durán et al. (2022). (**B**) Crustal thickness distribution between the northern lowlands and southern highlands on Mars. S1222a and the lander locations are denoted by yelllow and white symbols, respectively. Background colormap denotes the crustal thickness used for generating our 3-D crustal velocity model of Mars. Dichotomy boundary (yellow dashed) is based on Andrews-Hanna et al. (2008). SEIS = InSight seismometer; GCP = Great circle path

3 Result and Discussion

Our LP (∼30 s) vertical-component envelope shows strong amplitude signals in the predicted time windows for R1, R2, and R3 traveling with an average group velocity range of 2.4-3.0 km/s (black curve, Fig. 2A). Weaker and more localized later-arrivals are observed within the predicted time windows for R4-R7. These arrivals appear to have relatively large elliptically-polarized energy in the vertical plane in the same period range (dashed brown, Fig. 2A). Linearly-polarized signals such as a small amplitude glitch (gray, Fig. 2A) or other body wave arrivals would show a negative correlation between envelope amplitude and the FDPA for Rayleigh waves. Arrivals outside the predicted windows may be associated with multipathing of the propagated surface waves in 3-D crustal structure or body-to-surface wave conversion. Whichever the case, these arrivals may have been contaminated by strong atmospheric noise as indicated by the lander modes (Dahmen et al., 2021) clearly visible during the 10-hour recording period (Fig. S1). For VLP (∼85 s), the envelope amplitude and the corresponding FDPA curve is highly correlated and both data show distinctive peaks observed up to the R6 window with a higher traveling speed of 3.6-4.0 km/s (Fig. 2B). Notably, the peak shown in the R3 window has the smallest amplitude and polarization across the peaks associated with R1-R6. The observed peak in the R7 window has a relatively large amplitude but is weakly polarized.

Averaging across the R2-R7 signals, we observe the strongest amplitude signals at 30 s and 85 s central periods, propagating with distinctively different group velocities of 2.9 km/s and 3.8 km/s, respectively, in both amplitude and polarization stacks (Fig. 2C-D). At 30 s, similar group velocities have been independently reported by other studies for the R2 and R3 arrivals in S1222a (Kim, Stähler, et al., 2022; Li et al., 2022; Panning et al., 2023). Unlike typical, smoothly-varying surface wave dispersion curves, as predicted by the existing 1-D models (e.g., Durán et al., 2022; Drilleau et al., 2022)(Fig. S2), the observed group velocities show an apparent jump at intermediate periods between 20 s and 100 s and do not appear to constructively interfere across multiple orbits of Mars (Fig. S3). Such abruptness in dispersion and the observed low and high velocities from the R2-R7 signals cannot be solely attributed by elliptically-polarized martian wind (e.g., Stutzmann et al., 2021) contaminating the data which is unlikely to be recorded with the apparent periodicity for both LP and VLP data. At much longer period between 100-200 s, a similar group velocity close to 3.8 km/s for the excitation of R2 has been reported by using ambient noise correlations (Deng & Levander, 2022). A normal mode study on Mars has also shown some potential excitation of the fundamental mode surface waves in comparable period ranges between 120-300 s (Lognonné et al., under review).

The predicted dispersion curves using a suite of 1-D models with varying crustal thickness illustrate that the two end-member group velocities at LP and VLP appear as a type of stationary phase or "Airy-phase" (Aki & Richards, 2002) across different periods (Fig. S4). Depending on crustal thickness in a model, however, the rise and fall of the velocities at intermediate periods will vary substantially and would not constructively interfere across multiple orbits of Mars. Such Airy-phase is often associated with the amplification of Rayleigh waves on Earth that can propagate for considerable distances across the continental crust (Ewing & Press, 1956) and mantle (Ewing & Press, 1954). The observation of Rayleigh waves traveling over multiple orbits on the seismic recording of a relatively small-magnitude quake (M_W^{ma} 4.6) suggests those stationary values of group velocities on Mars could be occurring close to 30 s and 85 s central periods.

Our 3-D wavefield simulations also show that large-scale variations in crustal thickness across the equatorial dichotomy are necessary to reproduce this behavior (Fig. S5-S6). Using our 3-D model, we find the spectra of the R2-R7 arrivals in synthetic waveform is largely discontinuous in time and frequency. This feature becomes more evident for Rayleigh waves propagating in higher-orbits beyond R3. The variation in amplitude

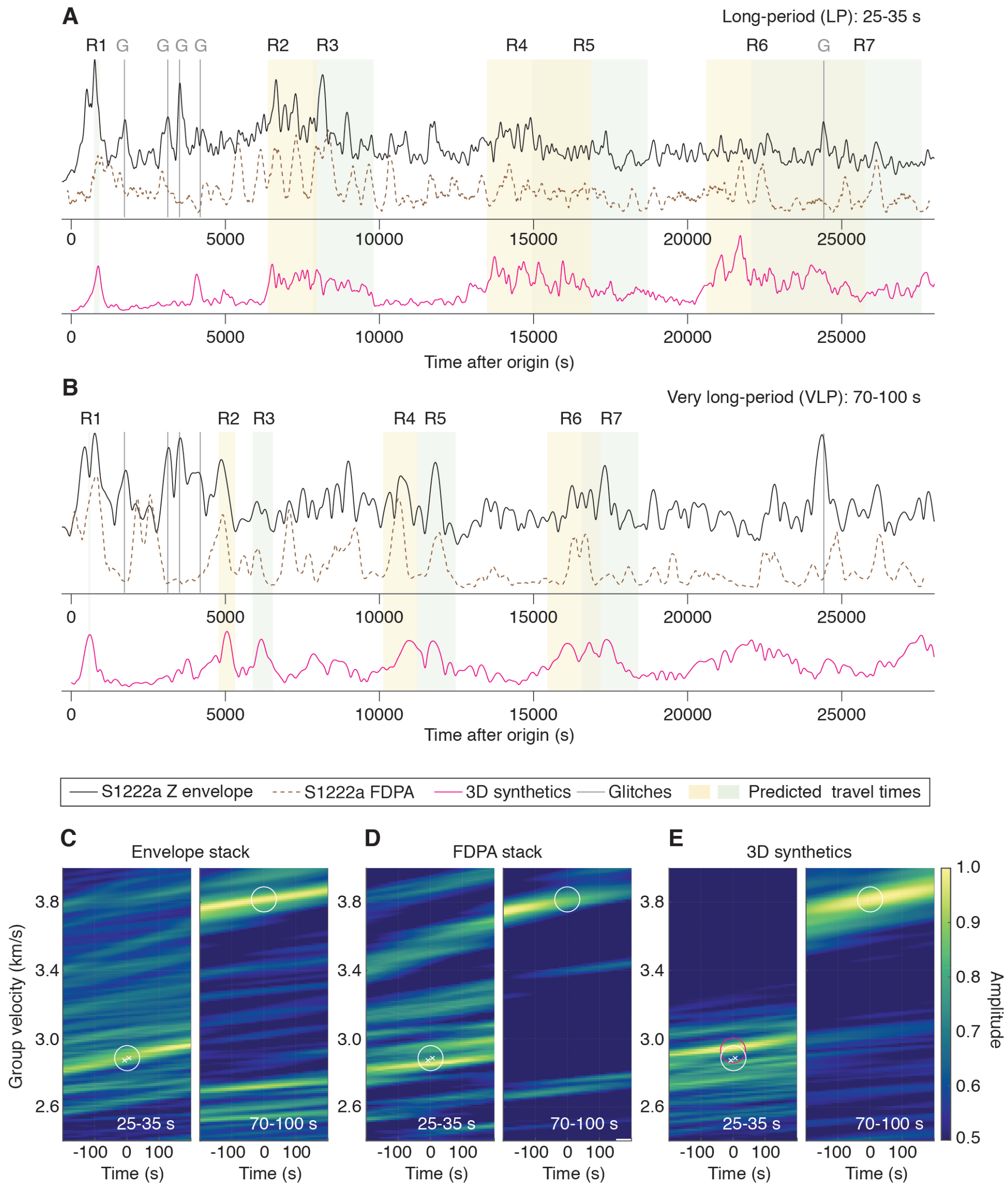

Figure 2. Vertical-component envelopes of the S1222a deglitched waveform (black) and FDPA (dashed brown) filtered between (**A**) 25-35 s (LP) and (**B**) 70-100 s periods (VLP). Shaded areas indicate the predicted time windows of R1-R7 arrivals base on the group velocities ranging from 2.4-3.0 km/s to 3.6-4.0 km/s for LP and VLP data, respectively. Glitches are shown by gray lines. Envelopes in magenta are based on a 3-D wavefield simulation using the model with crustal thickness variation shown in Fig. 1. Group velocity measurements of R2-R7 (white and magenta circles) are obtained by Nth-root stacking of the time-series in (A-B) for (**C-D**) data and (**E**) synthetics. White crosses are from independent analyses of R2 and R3 by Kim, Stähler, et al. (2022). See Fig. S3 for the complete analysis between 25-100 s with narrow-band filters. G = glitches; FDPA = frequency dependent polarization attribute

of surface waves propagating toward the minor-arc vs. major-arc directions (i.e., R_{odd} vs. R_{even}) also supports the evidence for lateral variation in crustal structure, likely due to (de)focusing of those waves (e.g., Romanowicz, 1987). Therefore, our observation of the absence of dispersion between ∼30-85 s for R2-R7 in S1222a and their associated amplitude change substantiate the choice of our 3-D model with large variation in crustal thickness (i.e., 20-90 km)(Fig. 1B) as these observations cannot be explained by existing 1-D models assuming a constant crustal thickness (Fig. S2).

The group velocity obtained for the largest amplitudes seen in the synthetic LP stack is consistent with our R2-R7 measurement of ∼2.9 km/s (with a small uncertainty of <2%; c.f., white and magenta symbols)(Fig. 2E), indicating that the average speed at which R2-R7 travel within the crust can be well-recovered with our 3-D model even with a large variation in crustal thickness (e.g., Fig. 1B). For the synthetic VLP stack, we find that the observed group velocity is strongly dependent on the versions of 1-D mantle models implemented in our analysis since the sensitivity of 70-100 s Rayleigh waves on Mars is predominantly between 75-115 km, a depth range in the uppermost mantle (Fig. S7). For example, the recent 1-D models produced by Durán et al. (2022) or Drilleau et al. (2022) have a 5% faster uppermost mantle than KKS21 (Fig. 1A). Our R2-R7 measurements are better fits to the newer sets of models that are based on a lower mantle FeO content compared to the KKS21 model that uses Wänke-Dreibus or Taylor compositions (Wänke et al., 1994; Taylor, 2013)(c.f., Fig. 2E and Fig. S8). This difference in seismic wavespeeds in existing models of the uppermost mantle, however, does not significantly affect body wave travel times with limited sensitivity and geographical coverage nor the estimated event locations (Fig. 3). Therefore, the new observations of R2-R7 provide a promising means of refining the 1-D models of the planet's radially symmetric structure, verifying the major element distribution of the martian mantle and determining the crustal thickness variations.

To find the average crustal thickness along the GCP from S1222a to the InSight lander, we carry out a systematic model-space search seeking average crustal V_S, thickness, and uppermost mantle V_S that fit the observed velocities of R2-R7 (Fig. 4A). We obtain a distribution of allowable velocities and thicknesses, with mean V_S of 3.38 km/s and 4.41 km/s for crustal and uppermost mantle, respectively, and a mean crustal thickness of 50 km beneath the GCP with an interquartile range between 44 and 58 km (magenta, Fig. 4A). This estimate of GCP-averaged crustal thickness and its uncertainty can be used as a robust anchoring-point and extrapolated globally using the existing models of crustal thickness based on gravimetric modeling (Wieczorek et al., 2022), which on their own suffer from a trade-off between average crustal density and thickness.

Crustal thickness directly beneath the lander based on RF analyses (Knapmeyer-Endrun et al., 2021; Kim, Lekić, et al., 2021) has previously been used as an anchoring-point to yield estimates of the average crustal thickness on Mars in the 30-72 km range. Here, we produce various crustal thickness models following the gravimetric modeling steps described in Wieczorek et al. (2022)(Fig. 4B). As an anchoring-point beneath the lander, we use the thickness of a three-layered crust ranging from 31 km to 47 km based on the previous RF analyses. Two end-member dichotomy structures with a uniform crustal density ranging from 2550 kg/m^3 to 3050 kg/m^3 (diamond symbol, Fig. 4B) and a model with a density contrast between 100-500 kg/m^3 across the dichotomy boundary have been tested (circle symbol, Fig. 4B). For the mantle and core beneath the lithosphere, we consider four plausible 1-D density profiles including both pre- and post-mission publications in Taylor (2013); Yoshizaki and McDonough (2020); Stähler et al. (2021); Khan et al. (2022).

Using the interquartile range of crustal thickness distribution along the GCP constrained by the R2-R7 analysis (magenta lines, Fig. 4A) against those from all models considered above, we were able to improve estimates of the average crustal thickness by ruling out the majority of those crustal models that have a >200 kg/m^3 density contrast

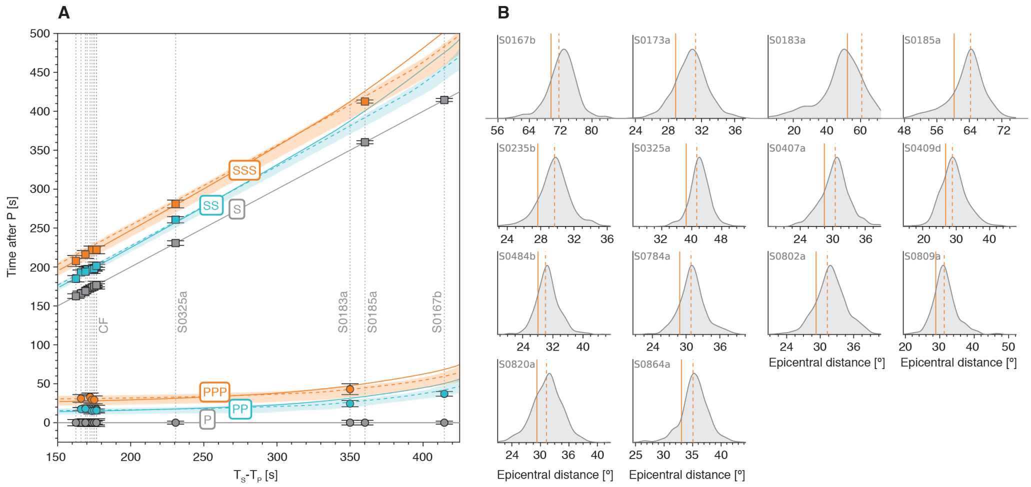

Figure 3. (**A**) Differential travel-time plot for available body wave measurements from quality A, B and C events and prediction by the inverted models of Durán et al. (2022)(shaded). Prediction by the composite models (Fig. 1B) with the mantle structure of KKS21 and the composite model with Duran2022 are shown by solid and dashed lines, respectively. Events are aligned by the their observed S-P travel time difference. Farside events (S0976a and S1000a; Horleston et al., 2022) are excluded since, besides the phases that allow for their alignment, no body-waves exclusive to the upper mantle and crustal structure were identified. CF = Cerberus Fossae event cluster. Note that the surface-reflected S-wave arrival (SS or SSS) of S0167b, categorized as a quality C event by the Marsquake Service (Clinton et al., 2021), was removed due to the lack of consensus on its nature (see Khan et al., 2021; Durán et al., 2022). (**B**) Distribution of the event distances from the inverted models in (Durán et al., 2022) (gray). Solid and dashed lines indicate the corresponding epicentral distances for the composite models (Fig. 1B) by fitting the predicted S-P travel times.

across the dichotomy (Fig. 4B). As a result, we obtain an estimate of the global average crustal thickness range between 42-56 km from the remaining models (symbols in magenta, Fig. 4B), which is a significantly narrower range than previously available. This implies large differences in crustal thickness between the northern lowlands and the southern highlands (up to ∼30 km), and places new constraints on the average global thickness of the martian crust, evidently thicker than the terrestrial (Dziewonski & Anderson, 1981; Huang et al., 2013) and the lunar crusts (Wieczorek et al., 2013) (Fig. 4C).

Of the major rocky bodies in the inner solar system for which constraints are available, Mars very likely has the thickest crust (i.e., 42-56 km). Based largely on seismic data, Earth's crust averages only about 24 km in thickness. The thickness of the lunar crust, which is anchored by Apollo seismic data, is in the range of 34-43 km (Wieczorek et al., 2013)(Fig. 4C). For the other bodies, there are no seismic data and crustal thickness constraints are based solely on gravity and topography measurements. Nevertheless, it is likely that on average, the thickness of the venusian crust is in the range of about 8-26 km (James et al., 2013; Maia & Wieczorek, 2022) and the mercurian crust in the range of 17-53 km (Padovan et al., 2015) or possibly even thinner (15-37 km; Sori, 2018). Even the crust of 4-Vesta may be broadly in this range with one estimate at 24 km (Ermakov et al., 2014). Accordingly, variations in crustal thicknesses of these rocky bodies appear to be within a factor of about 3-4 (McLennan, 2022). This is in contrast to planetary crustal masses which vary by well over an order of magnitude relative to the size of their

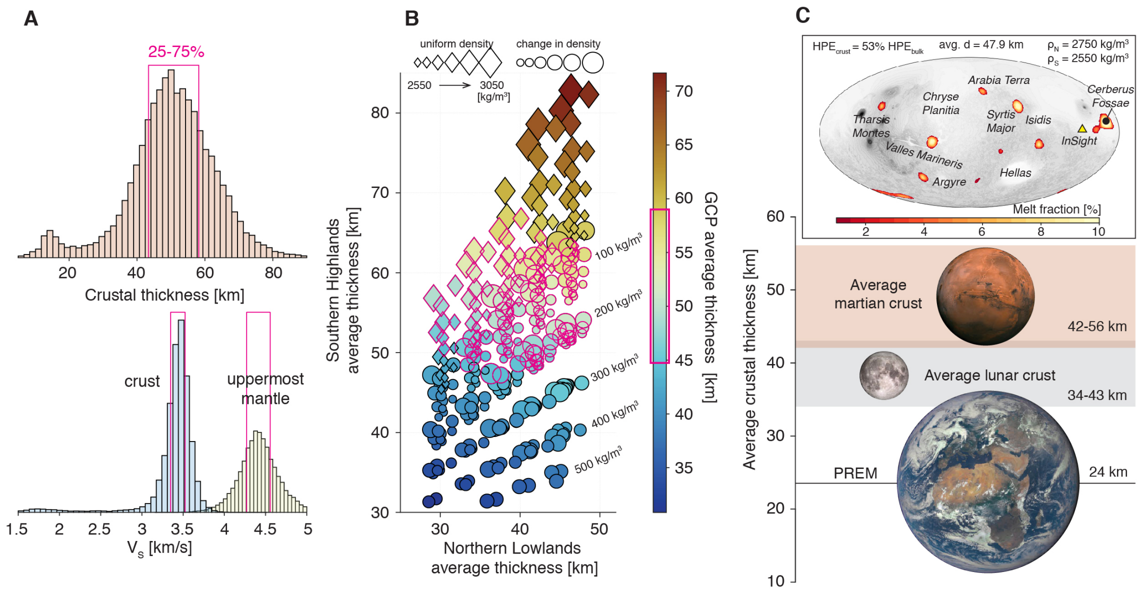

Figure 4. (**A**) Posterior distribution of the crustal and mantle V_S and crustal thickness along the GCP of S1222a. Interquartile range of the distribution is shown by red outlines. (**B**) Average crustal thickness of northern lowlands vs. southern highlands for global crustal thickness models with crustal densities ranging from 2550-3050 kg/m^3 with (circle symbol) and without a density contrast (diamond symbol) across the dichotomy. Dichotomy boundary is based on Andrews-Hanna et al. (2008). Colormap denotes the mean crustal thickness along the GCP for each model. Those models within the red outline are compatible with the posterior distribution in (A). (**C**) New global average crustal thickness range obtained by the model selection in (B) in comparison to that of the Earth and the Moon where constraints based on seismic data are available. Inset shows the best-fitting thermal evolution model of Plesa et al. (2018) computed with the new crustal constraint in (C). PREM = Preliminary Reference Earth Model. HPE = Heat-producing element

respective primitive mantles, between about 0.6% for Venus (and a similar value of 0.7% for Earth; Huang et al., 2013) to as much as 9.5% for Mercury and 14% for 4-Vesta (McLennan, 2022). Our results are consistent with Mars being intermediate among these values with the crust representing about 4-5% of the primitive mantle mass. Therefore, the degree of silicate differentiation into planetary crusts is more a function of overall planetary size than to crustal thickness and smaller bodies tend to have thicker crusts and increased degrees of mantle processing to form those crusts (O'Rourke & Korenaga, 2012; McLennan, 2022).

The tighter constraints on the crustal thickness obtained here compared to previously derived values from the RF analysis (Knapmeyer-Endrun et al., 2021) provide important information for thermal evolution models of the interior of Mars (Plesa et al., 2018, 2021; Khan et al., 2021; Knapmeyer-Endrun et al., 2021; Plesa et al., 2022). Together, this can help to further refine the president-day temperature distribution and amount of heat-producing elements within the crust. Thermal evolution models produced by using a maximum density contrast of $<$200 kg/m^3 across the dichotomy constrained by the R2-R7 analysis show that more than half of the total heat production but less than 70% of the total heat source budget needs to be in the crust, due to enrichment in the concentrations of Th, K, and U, in order to produce local melt zones in the mantle at present day (see detailed results in Fig. S9-S10). This crustal heat production range is consistent with the study of Knapmeyer-Endrun et al. (2021). For three end-member crustal models tested in Fig. S9-S10, we obtained enrichment factors between 8.2-14.3 (corresponding to a crustal heat production of 46.7-64.4 pW/kg). These enrichment factors are close to, but extend to slightly larger values than the enrichment estimated from GRS data 8 - 10.3 (crustal heat production of 46-51 pW/kg; Hahn et al., 2011). Interestingly, our best-fitting model with a 200 kg/m^3 variable density favors mantle plumes that can produce melt up to the present day in and around Cerberus Fossae (inset, Fig. 4D), supporting the interpretation from gravity and topography data (Broquet & Andrews-Hanna, 2022) and from seismic observations (Stähler et al., 2022). Therefore, our study offers a promising opportunity for further evaluating the plume hypothesis beneath Cerberus Fossae.

4 Open Research

The InSight event catalogue `https://doi.org/10.12686/a17` and waveform data are available from the IRIS-DMC `http://ds.iris.edu/ds/nodes/dmc/tools/mars-events/`, NASA-PDS `https://pds-geosciences.wustl.edu/missions/insight/seis.htm` and IPGP data center `https://doi.org/10.18715/SEIS.INSIGHT.XB_2016`.

Acknowledgments

This paper is InSight contribution number 315. The authors acknowledge the NASA, the CNES, their partner agencies and Institutions (UKSA, SSO, DLR, JPL, IPGP-CNRS, ETHZ, IC, and MPS-MPG) and the flight operations team at JPL, SISMOC, MSDS, IRIS-DMC, and PDS for providing the SEED SEIS data. Marsquake Service (MQS) operations at ETH are supported by ETH Research grant ETH-06 17-02. ETH authors recognize support from the ETH+ funding scheme (ETH+02 19-1: "Planet Mars"). V.L. acknowledge funding from NASA grant 80NSSC18K1628 and NASA Solar System Exploration Research Virtual Institute (SSERVI) Cooperative Agreement 80NSSC19M0216. SMM acknowledges funding from NASA grant 80NSSC18K1622.

References

Afanasiev, M., Boehm, C., van Driel, M., Krischer, L., Rietmann, M., May, D. A., ... Fichtner, A. (2019). Modular and flexible spectral-element waveform modelling in two and three dimensions. *Geophysical Journal International*, *216*(3), 1675–1692.

Aki, K., & Richards, P. G. (2002). *Quantitative seismology.*

Andrews-Hanna, J. C., Zuber, M. T., & Banerdt, W. B. (2008). The borealis basin and the origin of the martian crustal dichotomy. *Nature*, *453*(7199), 1212–1215.

Banerdt, W. B., Smrekar, S. E., Banfield, D., Giardini, D., Golombek, M., Johnson, C. L., ... et al. (2020). Initial results from the insight mission on mars. *Nature Geoscience*, *13*(3), 183–189.

Banfield, D., Spiga, A., Newman, C., Forget, F., Lemmon, M., Lorenz, R., ... et al. (2020). The atmosphere of mars as observed by insight. *Nature Geoscience*, *13*(3), 190–198.

Beghein, C., Li, J., Weidner, E., Maguire, R., Wookey, J., Lekić, V., ... Banerdt, W. (2022). Crustal anisotropy in the martian lowlands from surface waves. *Geophysical Research Letters*, *49*(24), e2022GL101508.

Broquet, A., & Andrews-Hanna, J. C. (2022). Geophysical evidence for an active mantle plume underneath elysium planitia on mars. *Nature Astronomy*, 1–10.

Ceylan, S., Clinton, J. F., Giardini, D., Stähler, S. C., Horleston, A., Kawamura, T., ... et al. (2022). The marsquake catalogue from insight, sols 0–1011. *Physics* *of the Earth and Planetary Interiors*, *333*, 106943.

Clinton, J. F., Ceylan, S., van Driel, M., Giardini, D., Stähler, S. C., Böse, M., ... et al. (2021). The marsquake catalogue from insight, sols 0–478. *Physics of the Earth and Planetary Interiors*, *310*, 106595.

Dahmen, N. L., Zenhäusern, G., Clinton, J. F., Giardini, D., Stähler, S. C., Ceylan, S., ... Banerdt, W. B. (2021, 10). Resonances and Lander Modes Observed by InSight on Mars (1–9 Hz). *Bulletin of the Seismological Society of America*, *111*(6), 2924-2950. doi: 10.1785/0120210056

Deng, S., & Levander, A. (2022). Autocorrelation r2 on mars. *Geophysical Research Letters*, *49*(17), e2022GL099580.

Drilleau, M., Samuel, H., Garcia, R. F., Rivoldini, A., Perrin, C., Michaut, C., ... et al. (2022). Marsquake locations and 1-d seismic models for mars from insight data. *Journal of Geophysical Research: Planets*, *127*(9), e2021JE007067.

Durán, C., Khan, A., Ceylan, S., Zenhäusern, G., Staehler, S., Clinton, J., & Giardini, D. (2022). Seismology on mars: An analysis of direct, reflected, and converted seismic body waves with implications for interior structure. *Physics of the Earth and Planetary Interiors*, *325*, 106851.

Dziewonski, A. M., & Anderson, D. L. (1981). Preliminary reference earth model. *Physics of the earth and planetary interiors*, *25*(4), 297–356.

Ermakov, A. I., Zuber, M. T., Smith, D. E., Raymond, C. A., Balmino, G., Fu, R. R., & Ivanov, B. A. (2014). Constraints on vesta's interior structure using gravity and shape models from the dawn mission. *Icarus*, *240*, 146–160.

Ewing, M., & Press, F. (1954). An investigation of mantle rayleigh waves. *Bulletin of the Seismological Society of America*, *44*(2A), 127–147.

Ewing, M., & Press, F. (1956). Rayleigh wave dispersion in the period range 10 to 500 seconds. *Eos, Transactions American Geophysical Union*, *37*(2), 213–215.

Garcia, R. F., Daubar, I. J., Beucler, É., Posiolova, L. V., Collins, G. S., Lognonné, P., ... et al. (2022). Newly formed craters on mars located using seismic and acoustic wave data from insight. *Nature Geoscience*, *15*(10), 774–780.

Giardini, D., Lognonné, P., Banerdt, W. B., Pike, W. T., Christensen, U., Ceylan, S., ... Yana, C. (2020). The Seismicity of Mars. *Nat. Geosci.*. doi: 10.1038/s41561-020-0539-8

Hahn, B., McLennan, S., & Klein, E. (2011). Martian surface heat production and crustal heat flow from Mars Odyssey Gamma-Ray spectrometry. *Geophysical Research Letters*, *38*(14).

Horleston, A. C., Clinton, J. F., Ceylan, S., Giardini, D., Charalambous, C., Irving, J. C. E., ... Banerdt, W. B. (2022, 04). The Far Side of Mars: Two Distant Marsquakes Detected by InSight. *The Seismic Record*, *2*(2), 88-99. doi: 10.1785/0320220007

Huang, Y., Chubakov, V., Mantovani, F., Rudnick, R. L., & McDonough, W. F. (2013). A reference earth model for the heat-producing elements and associated geoneutrino flux. *Geochemistry, Geophysics, Geosystems*, *14*(6), 2003–2029.

InSight Marsquake Service. (2022). *Mars Seismic Catalogue, InSight Mission; V3 2020-07-01. ETHZ, IPGP, JPL, ICL, ISAE-Supaero, MPS, Univ Bristol. Dataset.* doi: https://doi.org/10.12686/a19

InSight Marsquake Service. (2023). *Mars seismic catalogue, insight mission; v13 2023-01-01.* ETHZ, IPGP, JPL, ICL, Univ. Bristol. Retrieved from `https://www.insight.ethz.ch/seismicity/catalog/v13` doi: 10.12686/a19

Irving, J., Antonangeli, D., Banerdt, B., Li, J., Bozdag, E., Stähler, S., ... Stutzmann, E. (2022, 01). First observations of seismic waves travelling through the martian core..

James, P. B., Zuber, M. T., & Phillips, R. J. (2013). Crustal thickness and support of topography on venus. *Journal of Geophysical Research: Planets*, *118*(4), 859–875.

Karakostas, F., Schmerr, N., Maguire, R., Huang, Q., Kim, D., Lekic, V., … others (2021). Scattering attenuation of the martian interior through coda-wave analysis. *Bulletin of the Seismological Society of America*, *111*(6), 3035–3054.

Kawamura, T., Clinton, J. F., Zenhäusern, G., Ceylan, S., Horleston, A. C., Dahmen, N. L., … Banerdt, W. B. (2022). S1222a - the largest marsquake detected by insight. *Geophysical Research Letters*, e2022GL101543. doi: https://doi.org/10.1029/2022GL101543

Khan, A., Ceylan, S., van Driel, M., Giardini, D., Lognonné, P., Samuel, H., … et al. (2021). Upper mantle structure of mars from insight seismic data. *Science*, *373*(6553), 434–438.

Khan, A., Sossi, P. A., Liebske, C., Rivoldini, A., & Giardini, D. (2022). Geophysical and cosmochemical evidence for a volatile-rich mars. *Earth and Planetary Science Letters*, *578*, 117330.

Kim, D., Banerdt, W., Ceylan, S., Giardini, D., Lekić, V., Lognonné, P., … et al. (2022). Surface waves and crustal structure on mars. *Science*, *378*(6618), 417–421.

Kim, D., Davis, P., Lekić, V., Maguire, R., Compaire, N., Schimmel, M., … et al. (2021). Potential pitfalls in the analysis and structural interpretation of seismic data from the mars insight mission. *Bulletin of the Seismological Society of America*, *111*(6), 2982–3002.

Kim, D., Lekić, V., Irving, J. C., Schmerr, N., Knapmeyer-Endrun, B., Joshi, R., … et al. (2021). Improving constraints on planetary interiors with pps receiver functions. *Journal of Geophysical Research: Planets*, *126*(11), e2021JE006983.

Kim, D., Stähler, S., Ceylan, S., Lekic, V., Maguire, R., Zenhäusern, G., … et al. (2022). Structure along the martian dichotomy constrained by rayleigh and love waves and their overtones. *Geophysical Research Letters*, e2022GL101666.

Knapmeyer-Endrun, B., Panning, M. P., Bissig, F., Joshi, R., Khan, A., Kim, D., … et al. (2021). Thickness and structure of the martian crust from insight seismic data. *Science*, *373*(6553), 438–443.

Li, J., Beghein, C., Lognonné, P., McLennan, S. M., Wieczorek, M., Panning, M., … Banerdt, W. B. (2022). Different martian crustal seismic velocities across the dichotomy boundary from multi-orbiting surface waves. *Geophysical Research Letters*, e2022GL101243.

Lognonné, P., Banerdt, W. B., Giardini, D., Pike, W. T., Christensen, U., Laudet, P., … et al. (2019). Seis: Insight's seismic experiment for internal structure of mars. *Space Science Reviews*, *215*, 1–170.

Lognonné, P., Schimmel, M., Stutzmann, E., Davis, P., Drilleau, M., Sainton, G., … Panning, B. W. B., M. P. (under review). Detection of mars normal modes from s1222 event and seismic noise. *Geophysical Research Letters*.

Lognonné, P., Banerdt, W., Pike, W., Giardini, D., Christensen, U., Garcia, R., … Zweifel, P. (2020). Constraints on the shallow elastic and anelastic structure of Mars from InSight seismic data. *Nat. Geosci.*. doi: 10.1038/s41561-020-0536-y

Maia, J. S., & Wieczorek, M. A. (2022). Lithospheric structure of venusian crustal plateaus. *Journal of Geophysical Research: Planets*, *127*(2), e2021JE007004.

McLennan, S. M. (2022). Composition of planetary crusts and planetary differentiation. In *Planetary volcanism across the solar system* (pp. 287–331). Elsevier.

Moulik, P., Lekic, V., Romanowicz, B., Ma, Z., Schaeffer, A., Ho, T., … others (2022). Global reference seismological data sets: multimode surface wave dispersion. *Geophysical Journal International*, *228*(3), 1808–1849.

O'Rourke, J. G., & Korenaga, J. (2012). Terrestrial planet evolution in the stagnant-lid regime: Size effects and the formation of self-destabilizing crust. *Icarus*, *221*(2), 1043–1060.

Padovan, S., Wieczorek, M. A., Margot, J.-L., Tosi, N., & Solomon, S. C. (2015). Thickness of the crust of mercury from geoid-to-topography ratios. *Geophysical*

Research Letters, *42*(4), 1029–1038.
Panning, M. P., Banerdt, W. B., Beghein, C., Carrasco, S., Ceylan, S., Clinton, J. F., ... Zenhäusern, G. (2023). Locating the largest event observed on mars with multi-orbit surface waves. *Geophysical Research Letters*, *50*(1), e2022GL101270. doi: https://doi.org/10.1029/2022GL101270
Park, J., Vernon III, F. L., & Lindberg, C. R. (1987). Frequency dependent polarization analysis of high-frequency seismograms. *Journal of Geophysical Research: Solid Earth*, *92*(B12), 12664–12674.
Plesa, A.-C., Bozdağ, E., Rivoldini, A., Knapmeyer, M., McLennan, S. M., Padovan, S., ... Spohn, T. (2021). Seismic velocity variations in a 3d martian mantle: Implications for the insight measurements. *Journal of Geophysical Research: Planets*, *126*(6), e2020JE006755. doi: https://doi.org/10.1029/2020JE006755
Plesa, A.-C., Padovan, S., Tosi, N., Breuer, D., Grott, M., Wieczorek, M., ... Banerdt, W. (2018). The thermal state and interior structure of Mars. *Geophysical Research Letters*, *45*(22), 12–198.
Plesa, A.-C., Wieczorek, M., Knapmeyer, M., Rivoldini, A., Walterova, M., & Breuer, D. (2022). Interior dynamics and thermal evolution of mars–a geodynamic perspective. *Geophysical Exploration of the Solar System*, *63*, 179–230.
Posiolova, L. V., Lognonné, P., Banerdt, W. B., Clinton, J., Collins, G. S., Kawamura, T., ... Zenhäusern, G. (2022). Largest recent impact craters on mars: Orbital imaging and surface seismic co-investigation. *Science*, *378*(6618), 412-417. doi: 10.1126/science.abq7704
Romanowicz, B. (1987). Multiplet-multiplet coupling due to lateral heterogeneity: asymptotic effects on the amplitude and frequency of the earth's normal modes. *Geophysical Journal International*, *90*(1), 75–100.
Rost, S., & Thomas, C. (2002). Array seismology: Methods and applications. *Reviews of geophysics*, *40*(3), 2–1.
Scholz, J.-R., Widmer-Schnidrig, R., Davis, P., Lognonné, P., Pinot, B., Garcia, R. F., ... Banerdt, W. B. (2020). Detection, analysis, and removal of glitches from insight's seismic data from mars. *Earth and Space Science*, *7*(11), e2020EA001317. doi: https://doi.org/10.1029/2020EA001317
Sori, M. M. (2018). A thin, dense crust for mercury. *Earth and Planetary Science Letters*, *489*, 92–99.
Stähler, S. C., Khan, A., Banerdt, W. B., Lognonné, P., Giardini, D., Ceylan, S., ... et al. (2021). Seismic detection of the martian core. *Science*, *373*(6553), 443–448.
Stähler, S. C., Mittelholz, A., Perrin, C., Kawamura, T., Kim, D., Knapmeyer, M., ... et al. (2022). Tectonics of cerberus fossae unveiled by marsquakes. *Nature Astronomy*, 1–11.
Stockwell, R. G., Mansinha, L., & Lowe, R. (1996). Localization of the complex spectrum: the s transform. *IEEE transactions on signal processing*, *44*(4), 998–1001.
Stutzmann, E., Schimmel, M., Lognonné, P., Horleston, A., Ceylan, S., van Driel, M., ... Spiga, A. (2021). The polarization of ambient noise on mars. *Journal of Geophysical Research: Planets*, *126*(1), e2020JE006545. doi: https://doi.org/10.1029/2020JE006545
Taylor, G. J. (2013). The bulk composition of mars. *Geochemistry*, *73*(4), 401–420.
van Driel, M., Ceylan, S., Clinton, J. F., Giardini, D., Horleston, A., Margerin, L., ... others (2021). High-frequency seismic events on mars observed by insight. *Journal of Geophysical Research: Planets*, *126*(2), e2020JE006670.
Wieczorek, M. A., Broquet, A., McLennan, S. M., Rivoldini, A., Golombek, M., Antonangeli, D., ... Banerdt, W. B. (2022). Insight constraints on the global character of the martian crust. *Journal of Geophysical Research: Planets*, *127*(5), e2022JE007298. doi: https://doi.org/10.1029/2022JE007298
Wieczorek, M. A., Neumann, G. A., Nimmo, F., Kiefer, W. S., Taylor, G. J.,

Melosh, H. J., … Zuber, M. T. (2013). The crust of the moon as seen by grail. *Science*, *339*(6120), 671-675. doi: 10.1126/science.1231530

Wänke, H., Dreibus, G., Wright, I. P., Cowley, S. W. H., Runcorn, S. K., & Southwood, D. J. (1994). Chemistry and accretion history of mars. *Philosophical Transactions of the Royal Society of London. Series A: Physical and Engineering Sciences*, *349*(1690), 285-293. doi: 10.1098/rsta.1994.0132

Yoshizaki, T., & McDonough, W. F. (2020). The composition of mars. *Geochimica et Cosmochimica Acta*, *273*, 137–162.

Geophysical Research Letters

Supporting Information for

Global Crustal Thickness Revealed by Surface Waves Orbiting Mars

D. Kim[1]*, C. Duran[1], D. Giardini[1], A-C. Plesa[2], S. C. Stähler[1,3], C. Boehm[1], V. Lekic[4], S. M. McLennan[5], S. Ceylan[1], J. F. Clinton[6], P. Davis[7], A. Khan[8], B. Knapmeyer-Endrun[9], M. P. Panning[10], M. Wieczorek[11], P. Lognonné[11]

[1]Institute of Geophysics, ETH Zürich, Zürich, Switzerland; [2]DLR, Institute of Planetary Research, Berlin, Germany, Physik-[3]Institut, University of Zürich, Zürich, Switzerland; [4]Department of Geology, University of Maryland, College Park, USA; [5]Department of Geosciences, Stony Brook University, Stony Brook, USA; [6]Swiss Seismological Service, ETH Zürich, Zürich, Switzerland; [7]Department of Earth, Planetary and Space Sciences, University of California, Los Angeles, CA, USA; [8]Institute of Geochemistry and Petrology, ETH Zürich, Zürich, Switzerland; [9]Bensberg Observatory, University of Cologne, Bergisch Gladbach, Germany; [10]Jet Propulsion Laboratory, California Institute of Technology, Pasadena, CA, USA; [11]Université de Paris, Institut de Physique du Globe de Paris, CNRS, Paris, France

Contents of this file

Figures S1 to S10

Introduction

The supporting information below includes:

- Raw 10-hour SEIS data of S1222a and its spectra (Fig. S1).
- Group velocity predictions from existing 1-D models (Fig. S2).
- R2-R7 analyses focusing on narrow-bands across 20-100 s period range (Fig. S3).
- Collection of group velocity dispersion curves with two extreme model cases (Fig. S4).
- Synthetic S1222a data generated by our 3-D wavefield simulations (Fig. S5-S6).
- Depth sensitivity kernels for Rayleigh waves in VLP (Fig. S7).
- R2-R7 analysis on LP & VLP with the mantle model of KKS21 (Fig. S8).
- Thermal evolution model of Plesa et al. (2018) computed with the new crustal constraint in the main text (Fig. S9-S10).

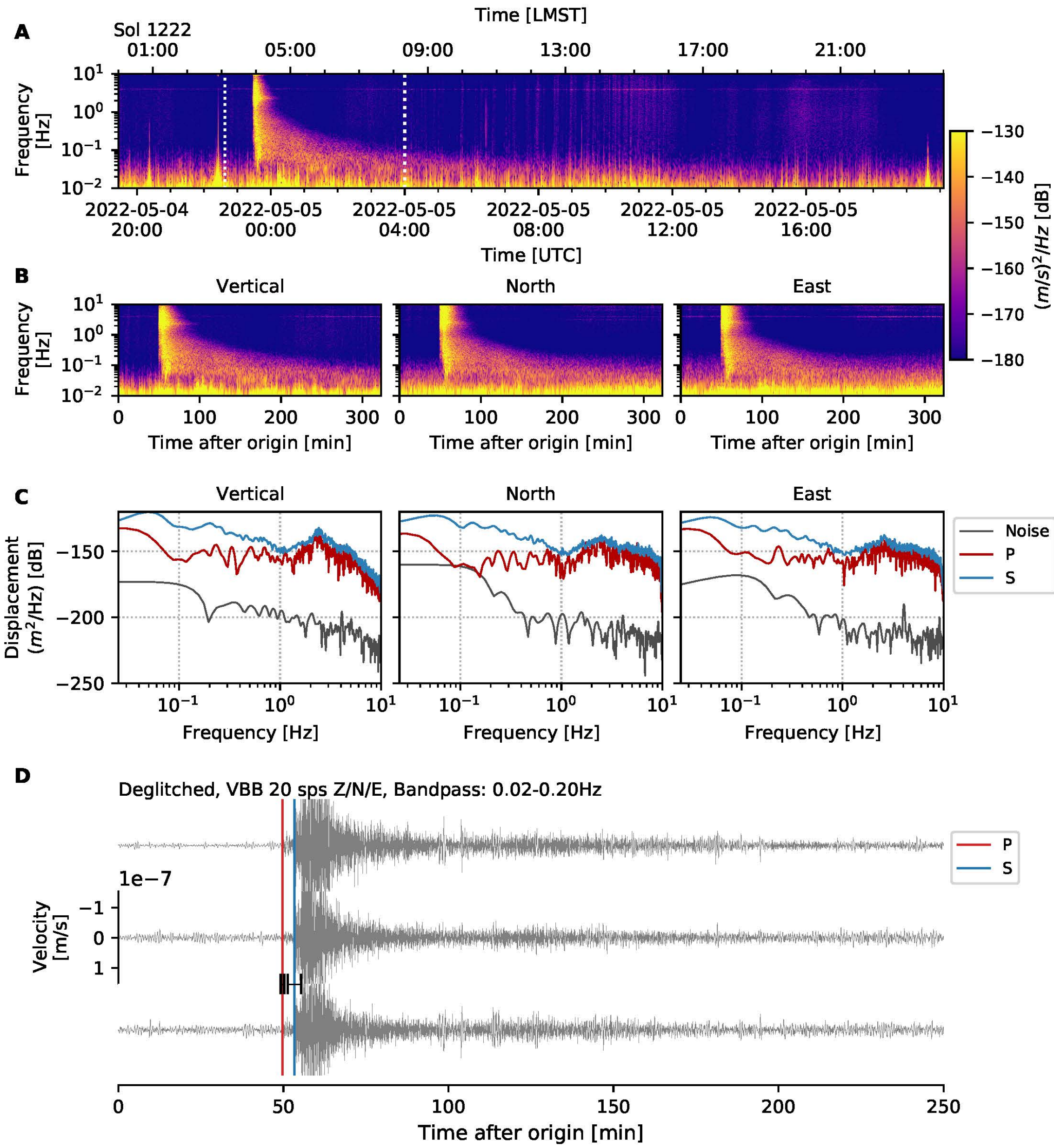

Figure S1. (**A**) One Sol long vertical-component velocity spectrogram of S1222a. (**B**) Three-component spectrograms zoomed into the event window as shown by the white dashed lines in (A). (**C**) Displacement spectra for P-, S-wave and the pre-event noise. Each spectra is computed based on the spectral time window reported by the MQS catalog. (**D**) Seismograms filtered between 0.02-0.2 Hz. Red and blue lines denote P and S arrival picks by the MQS, respectively. Uncertainties of those picks are marked by the black lines.

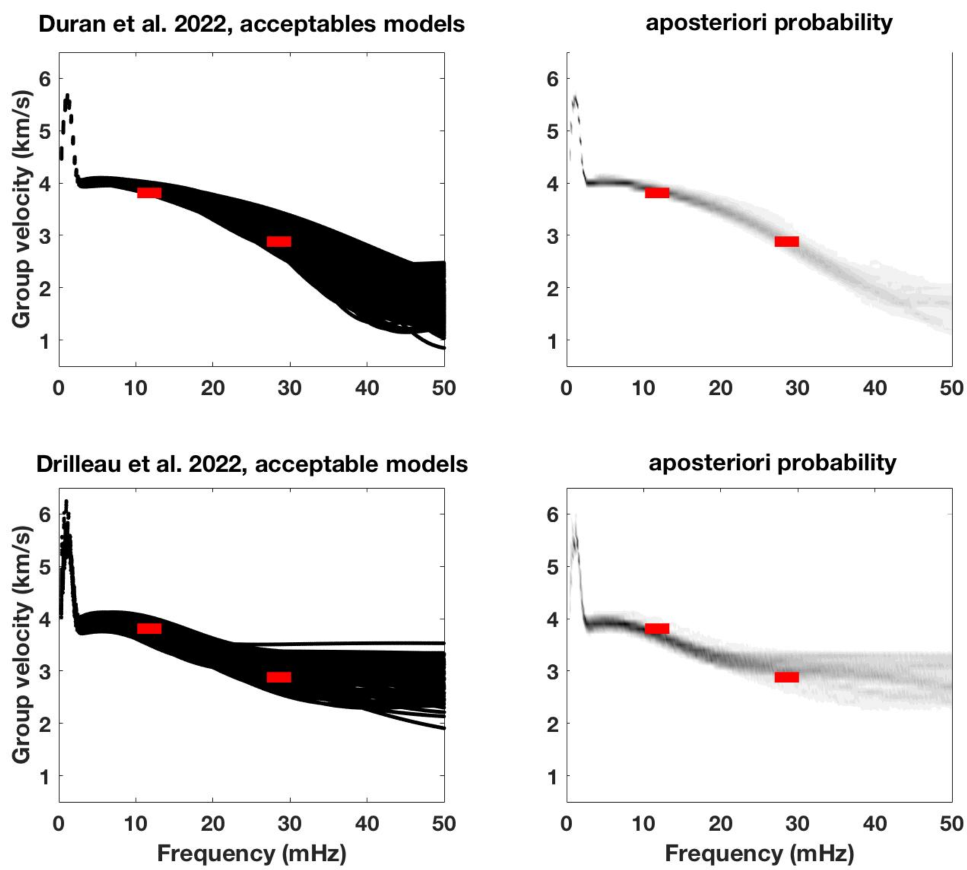

Figure S2. Group velocity predictions and their aposteriori probability made using 1000 acceptable models in Duran et al., (2022) (top row) and Drileau et al., (2022) (bottom row). Red markers denote the two distinctive group velocities observed at LP and VLP from the R2-R7 analysis discussed in the main text.

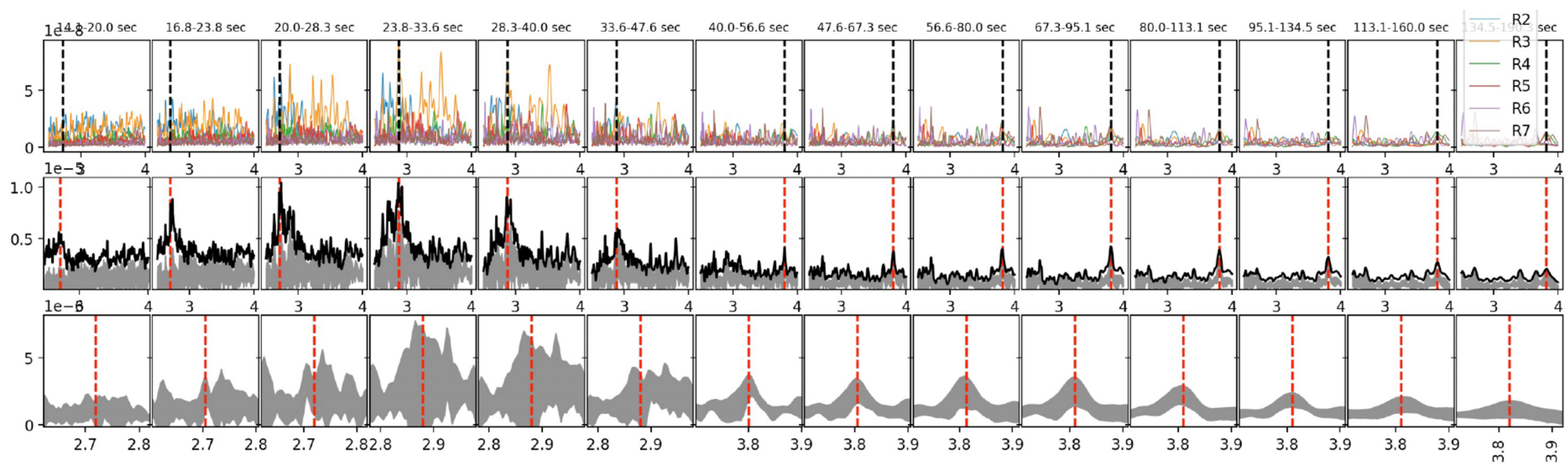

Figure S3. Individual vertical-component envelops (top row) and their 4-th root stack of the R2-R7 across different narrow period ranges between 20-100 s (middle row). Panels below show a zoom-in of those in the middle. Red dashed line denotes the largest amplitude signal in the stack.

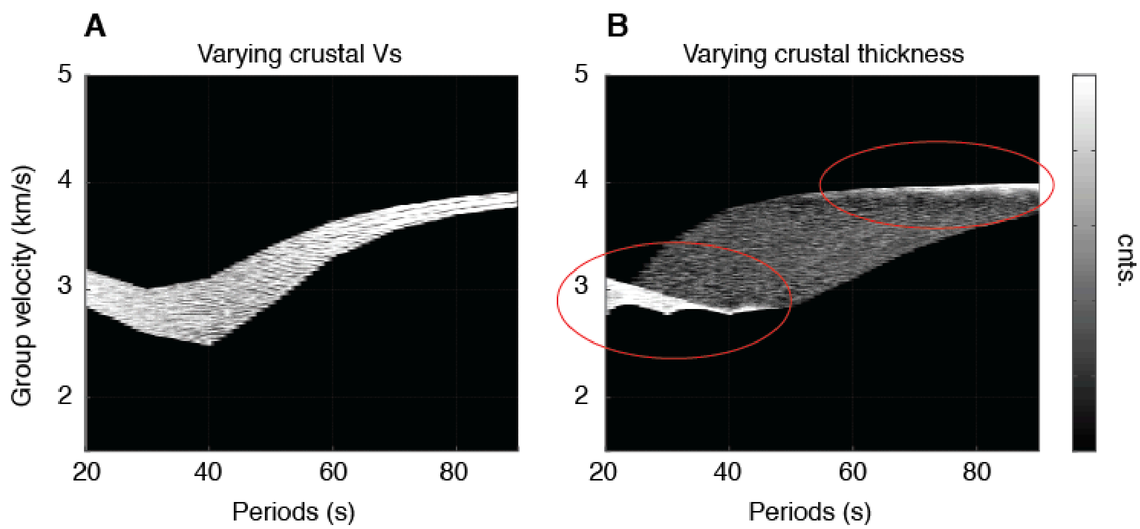

Figure S4. Group velocity predictions shown in a form of histogram for various 1-D models randomly produced by the posterior distribution of the crustal and mantle V_S and the crustal thickness in Duran et al., (2022) and Drileau et al., (2022). Two end-member model cases are tested: (**A**) the models of varying crustal V_S with a constant crustal thickness and (**B**) the models of varying crustal thickness with a constant crustal V_S. Note that for the models considered in (B), the two distinctive group velocities dominate the predicted dispersion curves as similarly observed in Fig. 2.

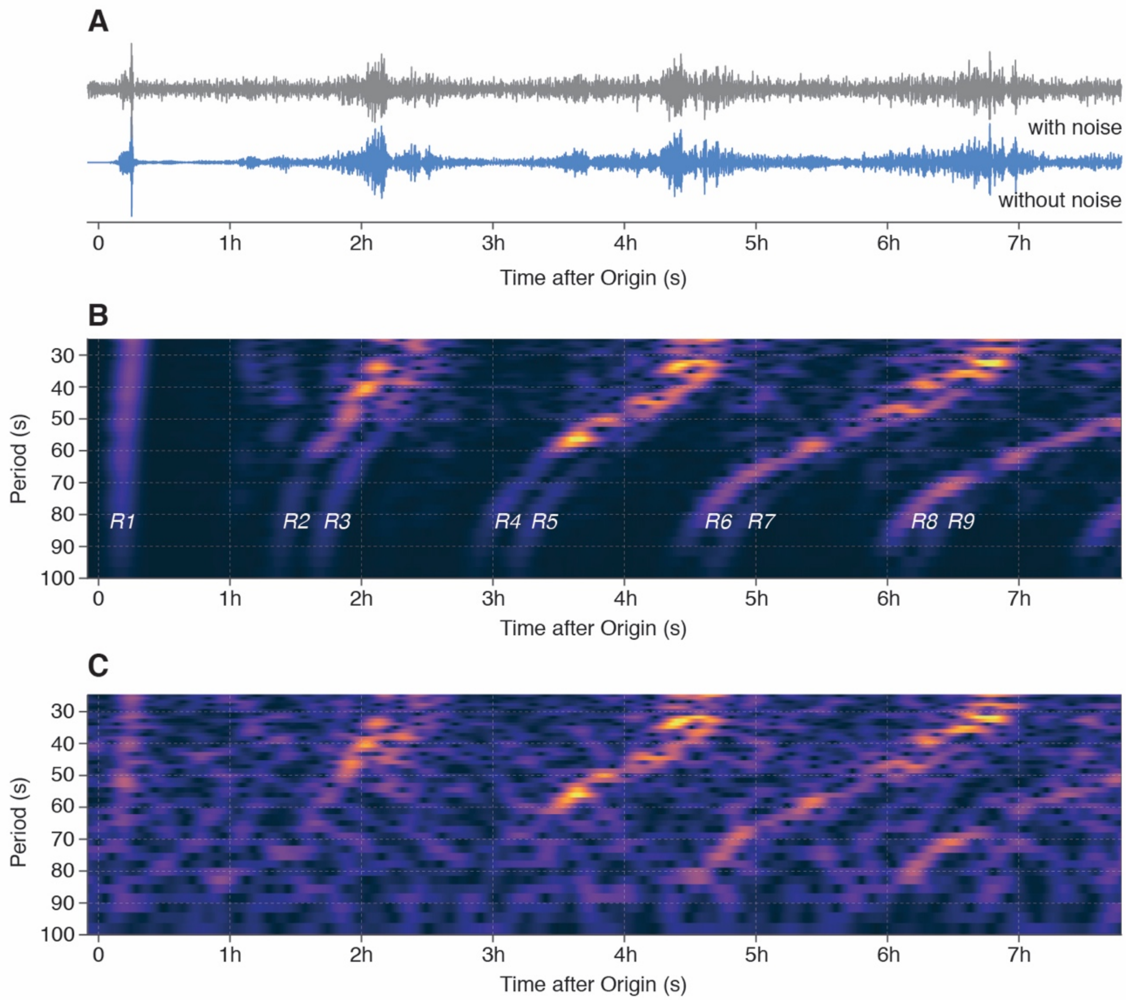

Figure S5. (**A**) 8-hour long vertical-component synthetic seismograms with and without the pre-event noise recorded in the data and (**B**-**C**) the corresponding spectrograms. 3-D wavefield simulation is performed using the 3-D crustal model overlying the mantle model of Duran et al., (2022) as discussed in the main text.

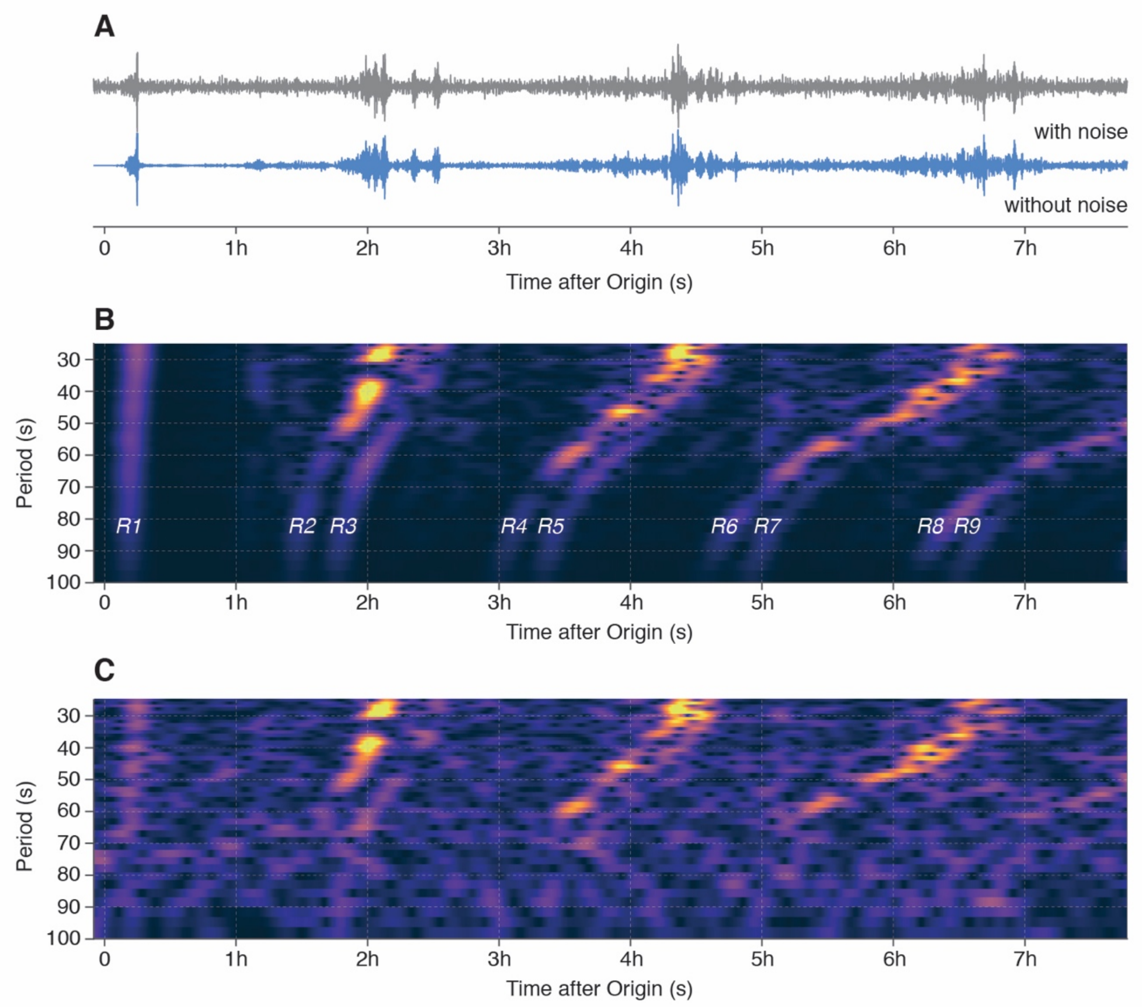

Figure S6. (**A**) 8-hour long vertical-component synthetic seismograms with and without the pre-event noise recorded in the data and (**B**-**C**) the corresponding spectrograms. 3-D wavefield simulation is performed using the 3-D crustal model overlying the mantle model of KKS21 as discussed in the main text.

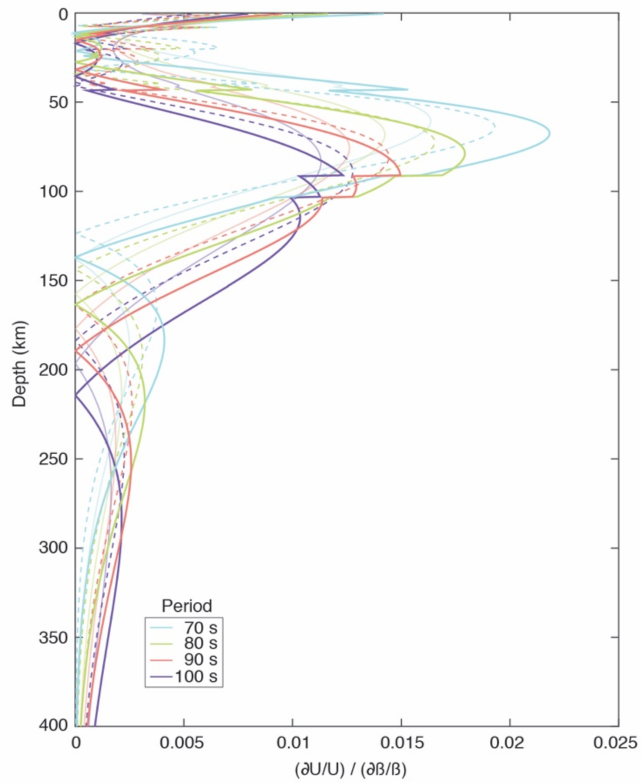

Figure S7. Depth sensitivity kernels for the fundamental mode Rayleigh waves in 70-100 s period range computed using different existing crustal velocity profiles on Mars (e.g., Knapmeyer-Endrun et al., 2021; Kim et al., 2022).

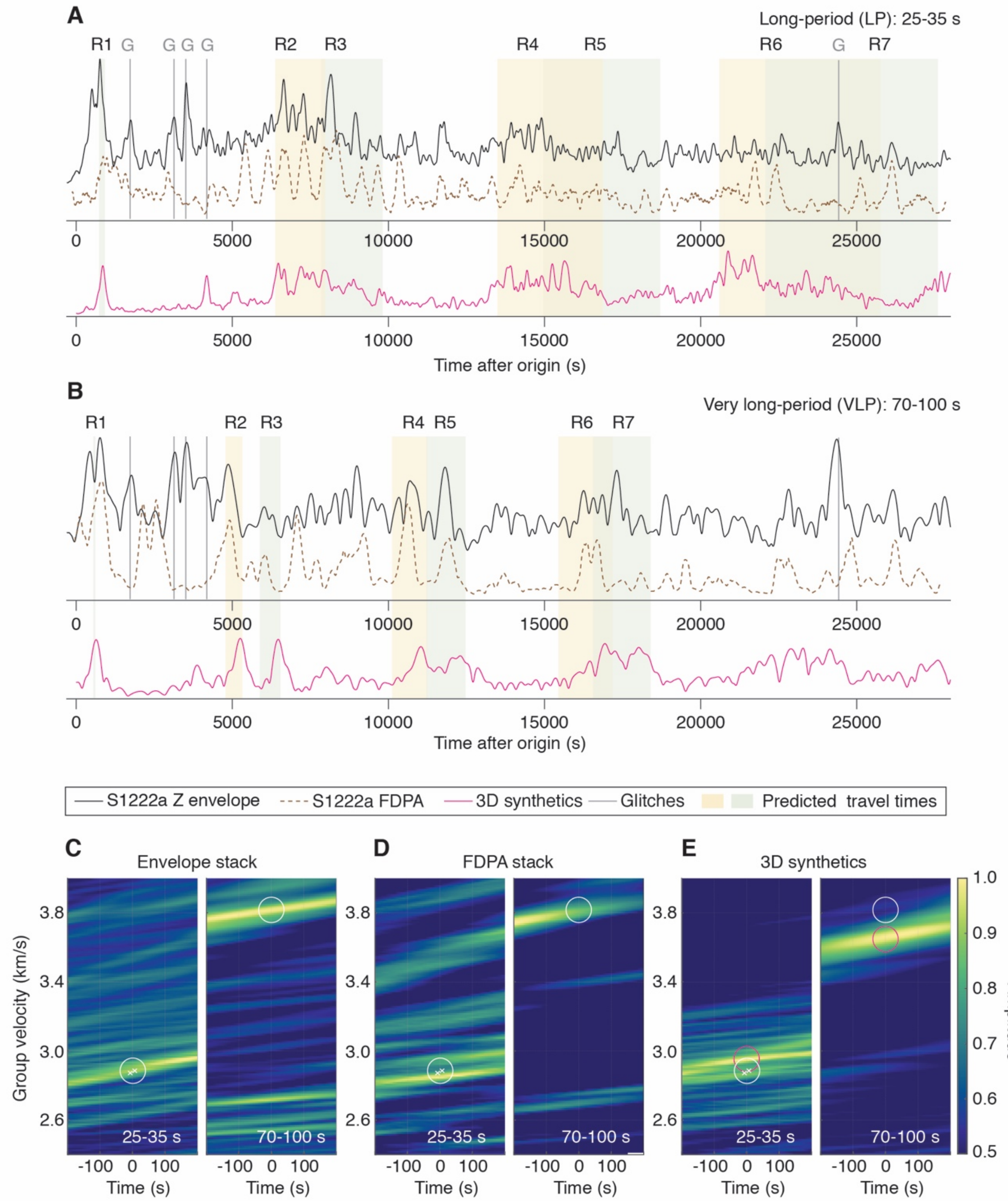

Figure S8. Same as Fig. 2 but the synthetic stack in (E) is based on the 3-D crustal model overlying the mantle model of KKS21(e.g., Fig. S6).

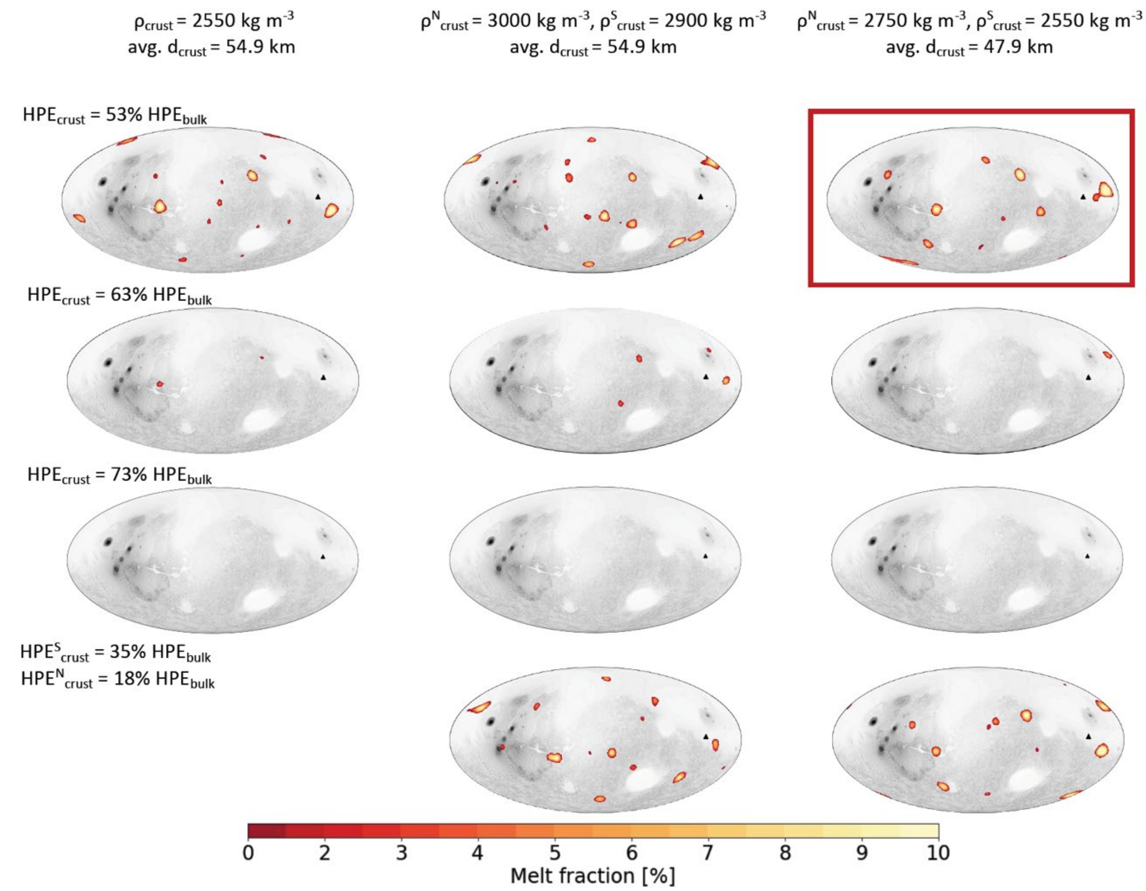

Figure S9. Distribution of partial melt produced by mantle plumes in the interior of Mars at present day. The left column shows the constant density models that employ an average crustal thickness of 55 km and contain 53%, 63%, and 73% of the total bulk content of radioelements in the crust. The middle and right column models have a small density difference of 100 kg/m^3 and 200 kg/m^3 between northern lowlands vs. southern highlands with an average crustal thickness of 55 km and 48 km, respectively. The mantle parameters are chosen as in Plesa et al., (2022). Best-fitting model is outlined in red which favors mantle plumes that can produce melt up to the present day in and around Cerberus Fossae.

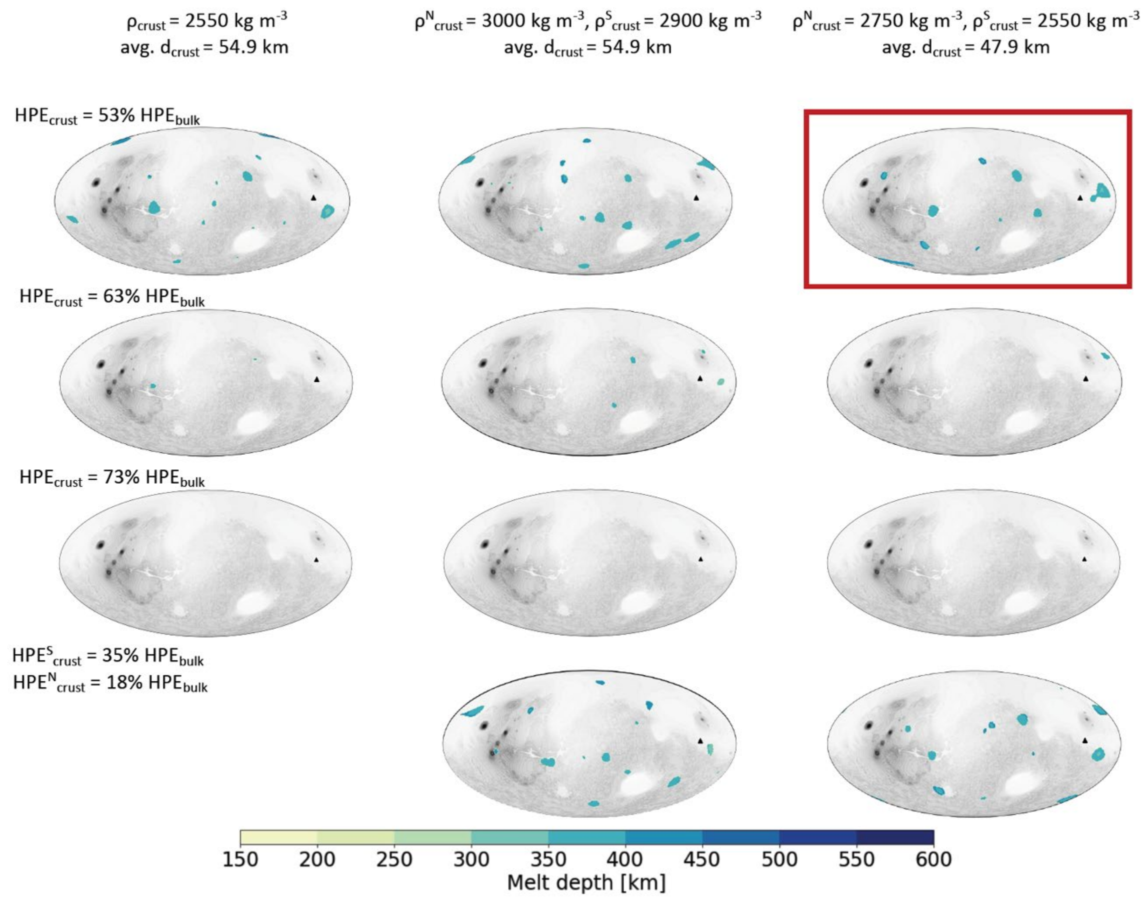

Figure S10. Distribution of the corresponding melt depth based on the models shown in Fig. S9. Best-fitting model is outlined in red which favors mantle plumes that can produce melt up to the present day in and around Cerberus Fossae.